Ice, Cloud, and land Elevation Satellite-2 (ICESat-2) Project

Algorithm Theoretical Basis Document (ATBD) for Inland Water Data Products ATL13 Version 003

March 1, 2020

by

Michael Jasinski, PI	*NASA GSFC*
Jeremy Stoll	*SSAI*
David Hancock	*SGT, Inc.*
John Robbins	*NASA GSFC*
Jyothi Nattala	*SGT, Inc.*
James Morison	*University of Washington*
Benjamin Jones	*University of Alaska*
Michael Ondrusek	*NOAA STAR*
Tamlin Pavelsky	*University of North Carolina*
Christopher Parrish	*Oregon State University*

and the ICESat-2 Science Team

Goddard Space Flight Center

Greenbelt, Maryland

Abstract

This document describes the theoretical basis of the algorithms employed in the derivation and processing of the ATL13 Inland Water Body Data Product for ICESat-2, Version 3. It supersedes Versions 1 and 2. Included are descriptions of the specific data products and product parameters, detailed algorithm steps required for the retrieval of those products, a summary of other ancillary ICESat-2 products required in the processing, and a calibration and validation plan.

Suggested citation for this ATL13 ATBD Version 003:

M. Jasinski, J. Stoll, D. Hancock, J. Robbins, J. Nattala, T. Pavelsky, J. Morrison, B. Jones, M. Ondrusek, C. Parrish, and the ICESat-2 Science Team, March 2020: *Algorithm Theoretical Basis Document (ATBD) for Inland Water Data Products, ATL13, Version 3*, Release Date March 1, 2020, NASA Goddard Space Flight Center, Greenbelt, MD, 112 pp. https://doi:10.5067/L870NVUK02YA. (March 2020)

Suggested citation when using ATL13 Inland Water data products from NSIDC:

M. Jasinski, J. Stoll, D. Hancock, J. Robbins, J. Nattala, T. Pavelsky, J. Morrison, B. Jones, M. Ondrusek, C. Parrish, and the ICESat-2 Science Team, 2020. *ATLAS/ICESat-2 L3A Inland Water Surface Height, Version 3*. [Indicate subset used]. Boulder, Colorado USA. NASA National Snow and Ice Data Center Distributed Active Archive Center. https://doi.org/10.5067/ATLAS/ATL13.003. (April 2020)

Acknowledgements

We gratefully acknowledge the numerous individuals who have made important contributions at various levels toward the development of the ATL13 Inland Water Data Products:

Tom Wagner, *NASA Headquarters*
Thorsten Marcus, *NASA Headquarters*
Jared Entin, *NASA Headquarters*
Woody Turner, *NASA Headquarters*
Tom Neumann, *NASA GSFC*
Lisa Callahan, *NASA*
Jeffrey Lee, *SGT, Inc.*
Kelly Brunt, *University of Maryland*
Kaitlin Harbeck, *SGT, Inc.*
Steve Palm, *SSAI*
Sinead Farrell, *University of Maryland*
Ron Kwok, *NASA JPL*
Ben Smith, *University of Washington*
Christopher Hiemstra, *CRREL*
Bill Cook, *NASA GSFC*
Christopher Arp, *University of Alaska*
Sabrina Delgado-Arias, *SSAI*
Bea Csatho, *University of Buffalo*
Huilin Gao, *University of Texas A&M*
Bernhard Lehner, *McGill University*
Anita Brenner, *SGT, Inc.*
Yao Li, *University of Texas A&M*
Jeffrey Danielson, *USGS*
Lori Magruder, *University of Texas ARL*
Eric Stengel, *NOAA STAR*
David Harding, *NASA GSFC*
Charon Birkett, *NASA GSFC*
Yongwei Sheng, *UCLA*
Jeremy Kasper, *University of Alaska*
Krista Bartz, *US National Parks Service*
Claudia Carabajal, *SGT, Inc.*
Jeffrey Gerber, *SGT, Inc.*
Mark Carroll, *NASA GSFC*
Jennifer Wozencraft, *JALBTCX*
Richard Kelly, *University of Waterloo*

CM Foreword

This document is an Ice, Cloud, and Land Elevation (ICESat-2) Project Science Office controlled document. Changes to this document require prior approval of the Science Team ATBD Lead or designee. Proposed changes shall be submitted in the ICESat-2 Management Information System (MIS) via a Signature Controlled Request (SCoRe), along with supportive material justifying the proposed change.

In this document, a requirement is identified by "shall," a good practice by "should," permission by "may" or "can," expectation by "will," and descriptive material by "is."

Questions or comments concerning this document should be addressed to:

ICESat-2 Project Science Office
Mail Stop 615
Goddard Space Flight Center
Greenbelt, Maryland 20771

Preface

This document is the Version 3 Algorithm Theoretical Basis Document for the ATL13 Inland Water Data Products processing implemented at the ICESat-2 Science Investigator-led Processing System (SIPS). It supersedes ATL13 Versions 1 and 2. The SIPS supports the ATLAS (Advance Topographic Laser Altimeter System) instrument on the ICESat-2 Spacecraft and encompasses the ATLAS Science Algorithm Software (ASAS) and the Scheduling and Data Management System (SDMS). The science algorithm software produces Level 0 through Level 3A&B standard data products as well as the associated product quality assessments and metadata information.

The ICESat-2 Science Team, in support of the ICESat-2 Project Science Office (PSO), assumes responsibility for this document and updates it, as required, as algorithms are refined or to meet the needs of the ICESat-2 SIPS. Reviews of this document are performed when appropriate and as needed updates to this document are made. Changes to this document will be made by complete revision.

Changes to this document require prior approval of the Change Authority listed on the signature page. Proposed changes shall be submitted to the ICESat-2 PSO, along with supportive material justifying the proposed change.

Questions or comments concerning this document should be addressed to:

Thomas Neumann, ICESat-2 Project Scientist
Mail Stop 615
Goddard Space Flight Center
Greenbelt, Maryland 20771

Review/Approval Page

Prepared by:

Michael F. Jasinski
ICESat-2 Science Team Lead for Hydrology and ATL13
Hydrological Sciences Laboratory, Code 617
NASA Goddard Space Flight Center
Greenbelt, MD 20771

Reviewed by:

Lori Magruder
ICESat-2 Science Team Lead
Applied Research Laboratories
University of Texas, Austin

Tom Neumann
ICESat-2 Project Scientist
Cryospheric Sciences Lab, Code 615
NASA Goddard Space Flight Center
Greenbelt, MD

Change History Log

Revision Level	Description of Change	SCoRe No.	Date Approved
1.0	**ATL13 Version 001**, Initial Release		May 28, 2019
2.0	**ATL13 Version 002** -Replaced GLWD with HydroLAKES. -Water bodies analyzed include: i) All transected lakes and reservoirs > 0.1 km^2 ii) Estuaries and bays iii) 7 km global coast buffer. - Implemented coarse bottom bathymetry algorithm for all water bodies, cloudiness and water clarity permitting. - Implemented dynamic shore finding algorithm		October 1, 2019
3.0	**ATL13 Version 003** -First photon bias (FPB) correction implemented using ATLAS CAL-19 procedure. -Wind speed estimated from standard deviation of water surface (*met_wind10_atl13*). -Updated water body shape file (ANC20) to include global river shapes. - Cloud confidence flag parameters retrieved from ATL09 and rescaled ATL13 at short segments.		March 1, 2020

3.0	**ATL13 Version 003 (Cont'd)** - Added downscaled ATL09 input wind vector components at 10m height (*met_u10m, met_v10m*). -Included bottom in determining the minimum height to calculate subsurface deconvolution. -Updated threshold counts of photons within short segment histogram multimode. -Included max available ATL03 geolocation segments outside of water mask edges, in height computation. -Added water body transect parameters; *transect_id, sseg_start_lat, sseg_start_lon, sseg_end_lat, sseg_end_lon* and *segment_azimuth*. -Corrected sign in EM bias (*H_bias_EM*) calculation. -Updated expression for orthometric water surface height and depth when *H_bias_EM* is designated as invalid and *H_bias_fit* designated as valid, to omit invalid term. -Implemented number of short segments to be designated as anomalous due to near-shore influences (*shore_buffer*). -Added surface (skin) temperature (*met_ts_atl09*) interpolated from ATL09 inputs at 1 Hz and 25 Hz rate. -Added NOAA snow/ice flag (*snow_ice_atl09*) from interpolation of ATL09. -Added writeup on MABEL Lake Mead bathymetry		March 1, 2020

List of TBDs/TBRs

Item No.	Location	Summary	Ind./Org.	Due Date

Table of Contents

List of Figures

List of Tables

1.0 INTRODUCTION

1.1 Purpose

This Algorithm Theoretical Basis Document (ATBD) of the Inland Water Body Height Data Product, consists of the Version 3 ATL13 processing algorithms produced from observations acquired by the ICESat-2 ATLAS sensor. It supersedes ATL13 Version 2 (Jasinski et al., October 2019a) and Version 1 (Jasinski et al., May 2019a). The ATL13 ATBD includes background (Chapter 2), details of the theoretical underpinnings of the algorithms together with their testing on ATLAS or ATLAS prototype data (Chapters 3 and 4), a list of the specific ATL13 output product tables (Chapter 5), and lists of calibration and validation background and opportunities (Chapter 6). Since this ATBD is refined over time due to improvement to the algorithms, a summary of the principal updates to each version or release is also provided below (Chapter 1).

1.2 Justification and Goals of ICESat-2 Inland Water Body Height Data Products

The Inland Water Body Height Data Product is computed as part of an integrated set of six ICESat-2 geophysical products that also include ice sheets, sea ice, atmosphere, vegetation structure and oceans. Climate variability is significantly impacting Arctic hydrology with regard to permafrost dynamics, lake extent and volume, snow accumulation and melt, and basin runoff (Rowland et al, 2010; Hinzman et al. 2005; IPCC, 2014; Serreze et al, 2000; Peterson et al., 2002). Consequently, time series observations of inland water heights and stores will allow a more complete understanding of the linkages among polar system dynamics and provide closure to the pan-Arctic water balance.

Inland water bodies are characterized by contiguous areas of surface water, with irregular disparate shapes spanning a wide range of sizes from small ponds to large inland lakes of $O(10^4)$ sq. km. Compared to open oceans, they possess distinct characteristics. For instance, they contain smaller waves and correspondingly higher water surface reflectances due to lower surface roughness. Inland water bodies are also prone to set-up on the lee shore with wave heights that are fetch dependent. Reflectance characteristics also differ. Inland water bodies generally exhibit unique color signatures and volume scattering characteristics of the local river basin, and greater mineral turbidity due to local runoff events and also under windy conditions due to resuspension of bottom sediments. Shallow depths of many inland and near shore water bodies result in a possible bottom backscatter component to the overall integrated water reflectance. In many regions of the world, seasonal weather and climate extremes can affect a water body's areal extent, which must be accounted for in the height retrieval algorithm.

ICESat-2 observations of inland water will i) enable understanding of the contribution of high-latitude hydrology and lake storage to the pan-Arctic water balance, and contribute to its associated impact on freshwater fluxes into the Arctic Ocean, melting snow, ocean salinity and circulation, methane distribution, ecosystem dynamics, and geomorphology, including the role of small lakes, ii) enable other science and application studies that may benefit from global, seasonal, high resolution Lidar observations of inland and near shore water body heights, such as shallow water bathymetry, and improved reservoir and water resources management, iii) provide geometric hydraulic properties for estimating stream discharge and lake storage/elevation/area relation, iv) serve as a high resolution calibration source for other radar altimeters, that generally perform poorly in ice covered lakes, and v) serve as an accurate high-resolution calibration for other radar altimeters, and provide synergy with the upcoming SWOT mission.

1.3 Definition of ATL13 Inland Water Body

The ATL13 Inland Water Body is defined as a contiguous continental water body of the following types: lakes and reservoirs greater than about 0.01km^2, rivers greater than about 100m, transitional water including estuaries and bays, and a near-shore 7km buffer. In aggregate, the number of water bodies defined above is globally 1.5 to 2.0 million. In ATL13, each water body is defined by a unique ID using publicly available masks and datasets. The project endeavors to include the most accurate and updated mask available, which also serves the advantage of being consistent with developments within future missions such as the Surface Water Ocean Topography (SWOT) mission

1.4 ATL13 Inland Water Along Track Data Product, Summary

The ATL13 data product provides the along-track water surface height products for each ATLAS beam. The principal products include the surface water height statistics (mean, standard deviation, slope), significant wave height, subsurface attenuation, and shallow bathymetry (when cloudiness and water clarity permit) as shown in Table 1-2. Additional secondary, supporting products are also computed as listed in Table 5-1. Version 3 data products were computed for global inland lakes greater to 0.10 km^2 traversed by ICESat-2 for which sufficient signal photons are recorded. While the domain of the ATL13 data product is global, the focus is on high-latitude terrestrial regions where the convergence of the ICESat-2 orbits provides spatially dense observations in the pan-Arctic region.

The target reporting scales of the ATL13 Inland Water Height data product are relatively short segment lengths with a minimum S-signal photons (E.g. Short segments, S=100 signal photon default), in order to observe as many small lakes as practical. The precise segment length depends on the number and quality of observations extracted from the along-track aggregation of

ATLAS observations that consist of signal and noise photons. A schematic representation of the Inland Water Height data product is shown in Figure 1-1. Each green segment represents an along track height, slope and rms product.

The frequency of water body crossings depends on the intersection of the water body mask and ICESat-2's orbital pattern that is characterized by a dual, latitude dependent observation strategy. For high latitude polar regions, mission requirements require that ICESat-2 repeats observations along the precisely established reference tracks, similar to ICESat-1. However, for all lower latitudes, ICESat-2 does not repeat during the first two years but rather implements s a systematic off-pointing mapping scenario. The frequency of observing a water body therefore depends also on its size and geographic location.

ATL13 water bodies are defined by a set of polygons in shape-file format.

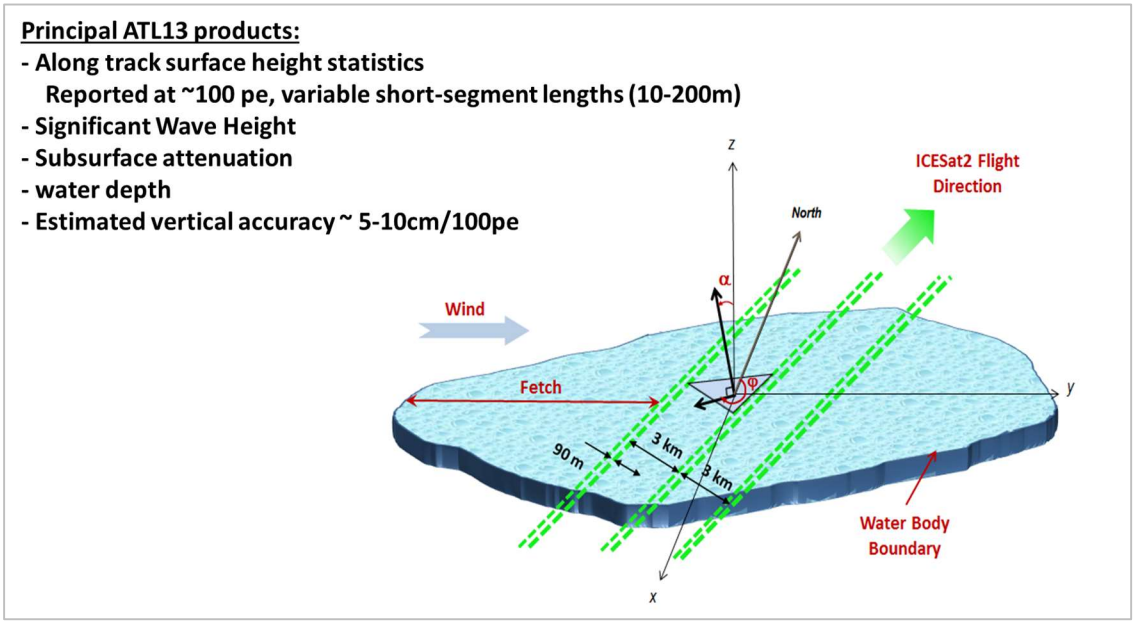

Figure 1-1 Schematic of principal ATL13 Inland Water Body along track data products includes surface height statistics, subsurface attenuation, significant wave height (SWH) and coarse bottom topography. Height statistics are reported for variable segment lengths of 100 signal photons.

The ATL13 product draws primarily from the Level 2 ICESat-2 ATL03 product. ATL03 includes: i) Precise latitude, longitude, and height for every received photon, arranged by beam in the along-track direction, ii) photons classified as signal or background, and also by surface

type (i.e., land ice, sea ice, land, ocean, inland water) including all geophysical corrections (e.g., Earth tides, atmospheric delay), and iii) photons segmented into several minute granules.

Given the low reflectance of water compared to other land and sea ice targets, the number of inland water surface signal photons ranges from about 0.5 to no more than several per meter (pe/m), based on early analysis of the MABEL data over Lake Mead, Chesapeake Bay, and the near shore Atlantic Ocean coast (Jasinski et al., 2016) and also confirmed with recent analysis of ATLAS data since launch in September 2018. It is expected that statistically representative inland water heights can be calculated over distances of a minimum of 10 to 100 m, depending on atmospheric, solar, and water conditions.

1.5 ATL13 Inland Water Along Track Data Product, Versions 001 to 003 Summary

The Inland Water Data Product is continually being updated to include new features and capability. Table 1-1 summaries the evolving features of progression of the data product through Versions 003 and future ATL22 releases. ATL13 products constitute along track height statistics across a water body transect. The list of all specific products associated with the latest ATL13 version is provided in Table 5.1.

Version	Release Date	Water Body Types (Number of unique IDs)	Description and Principal/Added Features
1	May 2019	Lakes & reservoirs > 10 km^2 (19,634)	- Surface water height statistics (mean, StdDev, slope), subsurface attenuation, and supporting variables at short segment length - Employs GLWD (Lehner & Doll 2004)
2	November 2019	Lakes & reservoirs $\geq$ 10 km^2 (19,800) Estuaries, bays, and near shore 7 km buffer (~3500)	- Replaces GLWD with HydroLAKES (Messager & Lehner, 2016) - Adds transitional waters Named Marine Water Bodies (ESRI) GSHHG Shoreline (Wessel et al, 1996) - Adds coarse bathymetry algorithm - Adds dynamic shore finding
3	March 2020	Lakes & reservoirs $\geq$ 0.1 km^2 (~1,400,000) Estuaries, bays, and near shore 7 km buffer (~3500) Rivers $\geq$ ~100 m wide (10,300)	- Uses GRWL (After Allen and Pavelsky, 2018) to create river mask shapes - Computes wind speed for all crossings - Adds Ice on/off flag from multi-sensor NOAA product - Corrects first photon bias error - Adds cloud confidence flag
ATL22	~July 2020	All water bodies	- Transect mean and supporting quantities

Table 1-1 Summary of Principal Features of the ATL13 Inland Water Data Product

1.6 Inland Water Transect Mean Products, ATL22

All ATL13 Data Products are reported at the along track, short-segment rate. The future Inland Water Data Product, or ATL22, is currently underway and will include mean transect and associated values as noted in Table 1-2 and in Table 5.2.

2.0 BACKGROUND

2.1 Summary of ICESat-2 ATLAS Instrument and Level 2 Data Products

NASA's Ice, Cloud, and land Elevation Satellite-2 (ICESat-2) mission is the second of the ICESat laser altimetry missions, projected to launch in September 2018. ICESat-2 carries an improved Advanced Topographic Laser Altimeter System (ATLAS) consisting of a low energy, micropulse, multibeam, high-resolution photon-counting laser altimeter possessing three pairs of beams. Each pair, separated by about 90 m, consists of a high energy (~100 mJ) beam and a low energy (25 mJ) beam each with an approximately 14 m footprint. Pairs of beams are separated by about 3 km. An instrument pulse rate of 10kHz and a nominal ground speed of ~7000m/s allow observations about every 70 cm. A schematic of the shot configuration is shown in Figure 2-1.

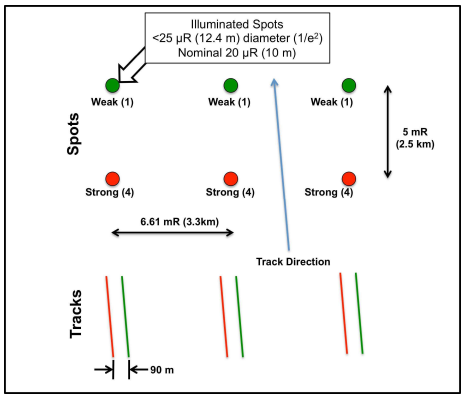

Figure 2-1 ICESat-2 ATLAS six-beam configuration.

ICESat-2/ATLAS is thus significantly different than its predecessor, ICESat/GLAS that fired at a much lower rate (40 Hz) but employed ~80 mJ lasers for full waveform detection (Abshire *et al*. 2005; Schutz *et al*., 2005). Each returned ATLAS photon is time-tagged with a vertical precision of approximately 30 cm, depending on surface and atmospheric characteristics. ATLAS also utilizes a narrower instrument FOV to limit the observation of solar photons. The ATLAS system thus provides higher measurement sensitivity with lower resource requirements. A summary of ATLAS parameters is shown in Table 2-1.

Parameter	**ATLAS**	**MABEL**
Operational altitude	500 km	20 km
Wavelength	532 nm	532 and 1064 nm
Telescope diameter	0.8 m	0.127 m
Laser pulse repetition frequency	10 kHz	Variable 5-25 kHz
Laser pulse energy	Strong beam: 121 μJ	Variable, nominal
	Week beam: 30 μJ	5-7 μJ per beam
Mean Pulse Width (FWHM)	< 1.5 ns	< 2.0 ns
Laser footprint diameter	17 m	100 μrad (2 m)
Telescope field of view		210 μrad (4.2 m)
Swath width	3.3 km	Variable up to 1.05 km
Inclination	94 deg	N/A

***Table 2-1 Summary comparison** of the principal ATLAS and MABEL instrument parameters.*

An additional unique feature of ICESat-2 is its two orbit modes. Above approximately +/-65 deg latitude, ATLAS operates in a repeat track mode over designated reference tracks similar to ICESat in order to obtain continuous time series of ice sheet change along those tracks. Below +/- 65 deg, however, ICESat-2 will systematically point left or right off the reference tracks in subsequent orbits, in order to conduct a two-year global mapping of vegetation. Additional scheduled off-pointing also is planned to observe targets of opportunity and calibration/validation sites.

2.2 Physics of Open Water

The retrieval of the inland water height requires consideration of several key physical processes including: i) the generation, characterization and statistical representation of surface waves, ii) the propagation and scattering of light, from both ICESat2 and sun sources, especially at the water surface and within the subsurface, and iii) an understanding of the characteristics of the satellite-based transmitted lidar pulse that interacts with the water, a portion that returns to the detector. These are briefly reviewed below and form the basis for the retrieval algorithm.

2.2.1 Dynamics of Inland Water Bodies

Water waves are generated by various mechanisms including wind, storms, seismic events and tides, as shown in Figure 2-2 below (Munk, 1950). Wind generated waves, however, including capillary and gravity waves, are the principal interest to ATL13 as their spatial scales of variability, from centimeters to tens of meters, are commensurate with the lidar observations and the desired Inland Water Body Height data product.

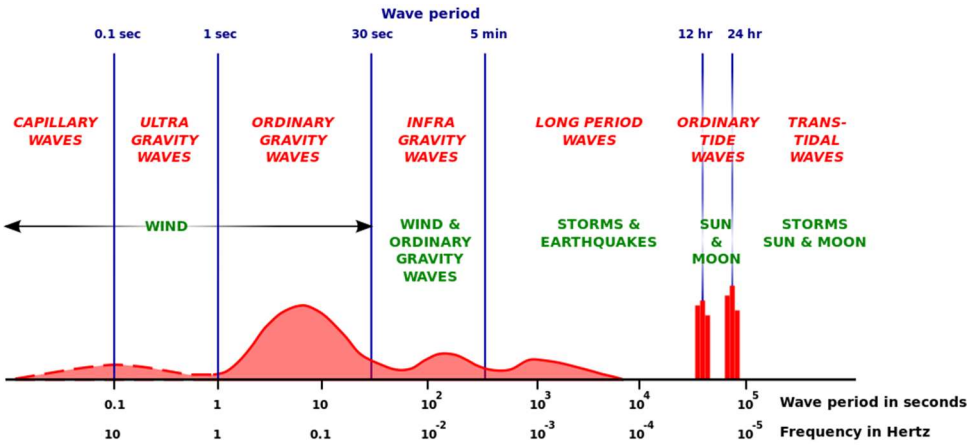

Figure 2-2 Classification of water wave types after Munk (1950).

The smallest water surface perturbations due to wind shear are relatively uniform capillary waves. Possessing short wavelengths of less than 2 cm, they are quickly dampened by the restoring force of surface tension at the cessation of wind. Capillary waves exhibit a rounded crest and a V-shaped trough. Although small, capillary waves play in important role in the retrieval algorithm as they form on flat surface and other gravity waves thus providing numerous facets for specular reflection of both the lidar beam and the sun.

Gravity waves are generated with continued and increasing wind force due to a combination of surface shear and form drag on the face of the wavy surface. Gravity waves exhibit wavelengths from about 10 cm to tens of meters. As their name implies, the restoring force is principally gravity with surface tension playing a small role at the shorter wavelengths. The magnitude of the lake gravity wave is a function of both the properties of the wind including speed, duration, direction, and persistence, and the geometry of the water body including shape, depth and fetch (upwind distance between observation and lee water body shore). As gravity waves approach a sloping shore, bottom friction causes them to slow down and steepen, and eventually break so to dissipate their energy.

A water body surface may exhibit any number of wave types depending on the history of wind events both locally and afar. Waves generated from distance sources that propagate to the region of interest, or that remain after cessation of the wind, are generally smooth in shape and often termed swells.

Waves are described in terms of wavelength (m), period (sec), wavenumber (radians/m) and angular frequency (radians/sec). Wave theories are often based in terms of wavelength and water depth parameter space, as shown in Figure 2-4. By definition, short wave or deep water

waves are characterized by a depth to wavelength ratio greater than one-half. Long waves or shallow water waves occur when the depth to wavelength ratio is less than one-half.

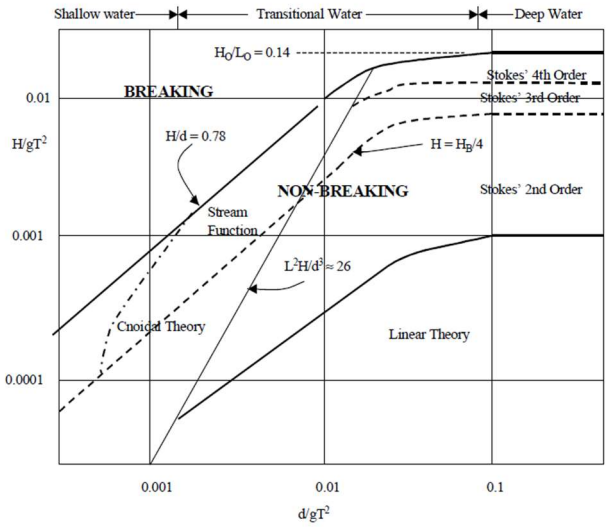

Figure 2-3 Parameter space for wave theories based on normalized height ($H/g\tau^2$) and water depth ($d/g\tau^2$), where g is gravity constant, and τ is wave period, after Le Méhauté, B. (1976).

Two additional properties of open water waves are the significant wave height and significant wave slope. Significant wave height, H_S, is defined the mean wave height (trough to crest) of the highest third of the waves, or equivalently, as four times the standard deviation of the surface height distribution. The significant slope is H_S/λ, where λ is the dominant wavelength. Bourassa et al (1981) described the relation among significant wave height, significant slope, and wind speed, as shown in Fig 2-4. Huang (1981) showed the importance of significant slope relative to mixed layer processes such as mixing efficiency and dissipation for higher frequency surface waves and breaking effects.

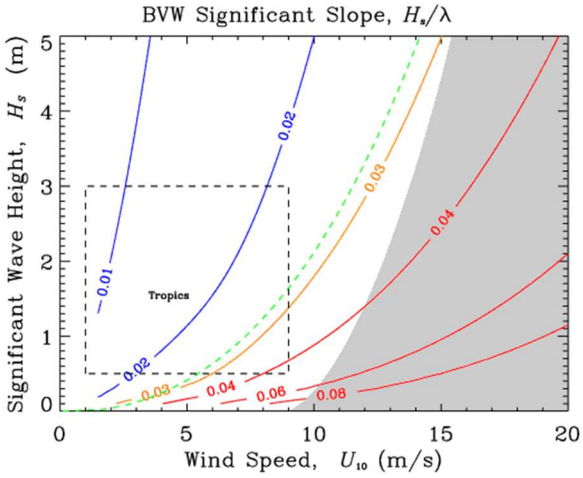

Figure 2-4 Relation among significant wave height, H_s, significant wave slope, H_s/λ, where λ is dominant wavelength, and wind speed U_{10}. Green line shows local-equilibrium values predicted by Bourassa et al. (1996) Blue and red lines represent falling (swells) and rising seas, respectively. (From http://coaps.fsu.edu/papers/use_significant_derived_stress/).

The shape and vertical distribution of open water gravity waves depend on numerous factors including the time history of local wind speed and direction, waves generated from distant sources, changes in water depth, and the reflection of waves from nearby obstacles and shorelines. Open water waves have often been depicted as sinusoidal or trochoidal (Gerstner, 1802; Rod Nave GSU; Bascom, 1964).

Certain simple waves, such as shallow waves approaching a shore, can be modeled explicitly. However, in reality, most wind generated waves are random and require a statistical representation, through the superposition of many waves. Statistically, it has been argued that a random wave field possesses can be modeled with a Gaussian pdf due to the Central Limit Theorem (Longuet-Higgins, 1975; Hu et al, 2008). Caulliez and Gerin (2012) reported on the importance of higher moments as a function of wind speed. Although conducted in a wind tank, they found that the smallest wind speeds yielded the most Gaussian shape.

Waves continue to grow with wind speed, duration and the distance or fetch over which it blows. Wind set-up, or the vertical rise in the water level on the lee side of a water body, as in Figure 2-5, is caused by sustained wind shear on the surface of the water. Set-up ranges from a few centimeters for small lakes to up to two meters for the Great Lakes. After cessation of the wind, lake oscillation or seiching can occur. The relationship between fetch and wind has received

significant attention in the literature (Hasselmann et al, 1973; Kahma, 1981, Donelan et al, 1985; Dobson et al, 1989, and Young et al, 1994; and Elfouhaily et al, 1997).

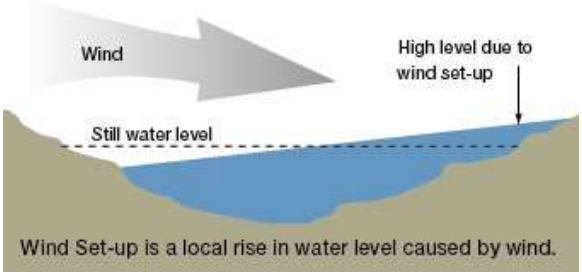

Figure 2-5 Representation of wind set-up due to prevailing winds (graphic from http://www.seagrant.umn.edu/superior/processes).

From the perspective of remote sensing, perhaps more important than surface height, is the slope distribution of the wave facets. Wave facets are critical, especially to optical remote sensing systems such as lidar, since they specularly reflect the majority of signal photons back to the detector. The statistical representation of wave slope has been the subject of much discussion in the literature (E.g. Cox and Munk, 1956; Liu et al., 1997; Ross et al., 2011).

Although published over 50 years ago, one of the most popular and still widely used statistical representations of the water surface slope distribution was proposed by Cox and Munk (1954). Using sun glint analysis, they formulated a near 2D Gaussian distribution or

$$P(Z_{up},Z_{cr})=\frac{1}{2\pi\sigma_{up}\sigma_{cr}}\exp\left(-\frac{\xi^2+\eta^2}{2}\right)$$

$$\times\left\{\begin{array}{l} 1 \quad -\frac{1}{2}c_{21}(\xi^2-1)\eta \\ \quad -\frac{1}{6}c_{03}(\eta^3-3\eta) \\ +\frac{1}{24}c_{40}(\xi^4-6\xi^2+3) \\ +\frac{1}{24}c_{04}(\eta^4-6\eta^2+3) \\ +\frac{1}{4}c_{22}(\xi^2-1)(\eta^2-1) \end{array}\right\} \tag{2.1}$$

where ξ and η are the standardized slope components in the up/downwind and crosswind directions, respectively, σ_{up} and σ_{cr} are the mean standard deviation of the slopes, respectively, and the c_n's are coefficients of five higher moment expansion terms resulting in a two-dimensional Gram Charlier distribution. The expansion terms represent kurtosis and peakedness in the distribution (Cox and Munk, 1953; Liu et al 1996; Breon and Henriot, 2006; many others).

Cox and Monk (1954) further demonstrated by empirical regression that σ_{up} and σ_{cr} are linearly related to wind speed height at 12.5 m (41 ft). One dimensional and composite versions also were formulated, or

$$\sigma_c^2 = 0.003 + 0.00192W \tag{2.2a}$$

$$\sigma_u^2 = 0.000 + 0.00316W \tag{2.2b}$$

$$\sigma_c^2 + \sigma_u^2 = 0.003 + 0.00512W \tag{2.2c}$$

where c_{21} = 0.01 - 0.0086W +/- 0.03, c_{03} = 0.04 - 0.033 +/- 0.12, c_{40} = 0.40 +/- 0.23, c_{22} = 0.12 +/- 0.06 and c_{04} = 0.23 +/- 0.41. Numerous investigators have proposed modifications or alternatives to the Cox and Munk formulations both theoretically and experimentally (Wu, 1990; Liu et al., 1997, Plant, 2007; Ross, 2007; Elfouhaily et al, 1997; Haltrin 2001; Hu et al., 2008; Breon and Henriot, 2006), although there still appears to be no universally acceptable formulation across the full range of sea states (Su et al, 2002), and some recent satellite studies still assume a Gaussian wave slope distribution (E.g. Hu et al, 2008). Minorov et al (2012) recently asserted that kurtosis increases significantly with wind and that slopes of deep-water waves exhibit much greater kurtosis than shallow water waves. Under a Gaussian assumption, the observations are

characterized only by the mean and standard deviation. However, additional cumulants were necessary to reproduce Stokes gravity waves, namely the skewness and kurtosis coefficients in order to take into account vertical asymmetry of waves and flatness of troughs (Minorov et al 2012).

2.2.2 Light Reflection and Transmission in Open Water

There exists extensive literature on light propagation in open water (E.g. Kirk, 1994; Mobley, 1994; and Bukata et al, 1995) including lidar (Churnside, 2014; Montes et al, 2011). The ability of photons to propagate through the water surface and into the water body depends on both the physical reflection properties at the surface governed by Fresnel scattering and wave facet scattering noted above, and the absorption and scattering properties of the water medium governed by various mineral and organic constituents.

The propagation of light within the water column has revealed unique signatures for oceans, coasts and inland estuaries as shown in Figure 2-6 below. As can be seen for 532 nm wavelength which is flown on ICESat-2, the open ocean photic zone representing Case I water can extend to nearly 80 m. However, in the coastal marine and estuary zones, or Case II water, typical light penetration is only up to about 20 m and 6 meters, respectively. Inland water penetration will depend on the clarity of the water body and can vary greatly, but is expected to be from a few meters in turbid water to several tens of meters in clear water.

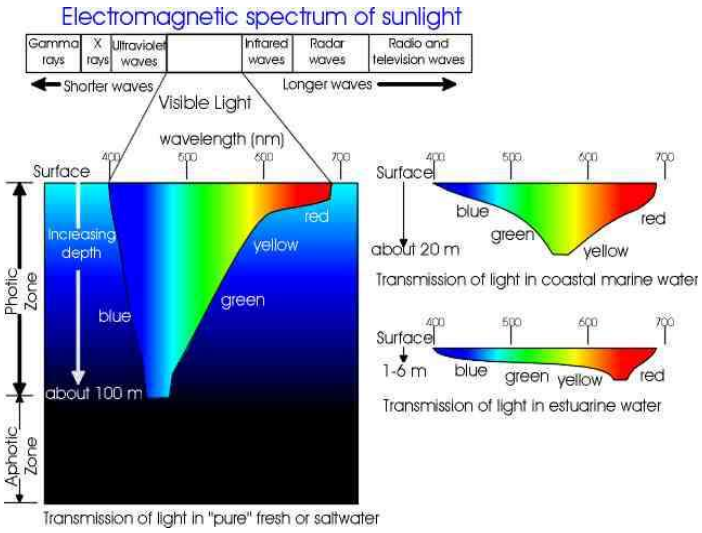

Figure 2-6 Comparative representation of light penetration in natural water including open ocean (left), coastal marine (top right) and estuary (bottom right). (from Buchheim, Oceanography http://www.marinebiology.org/oceanography.htm)

The optical properties of water can be specified in terms of its inherent optical properties (IOP) acting on a vertically stratified water medium. The main properties are wavelength dependent and include: i) the absorption coefficient $\alpha(\lambda)$ (m^{-1}), ii) the scattering coefficient $b(\lambda)$ (m^{-1}), iii) the attenuation coefficient $c(\lambda) = \alpha(\lambda) + b(\lambda)$, and iv) the scattering phase function $\beta(\lambda)$ (sr^{-1}) (Mobley, 1994). The scattering coefficient is often described in terms of forward and backward scattering. The total IOPs of a water body are usually represented as the sum of contributions from water itself and of pertinent optically significant constituents. Such constituents are generally divided into four classes: i) Phytoplankton cells and colonies (Phyt), ii) mineral suspended solids (MSS), iii) colored dissolved organic matter (CDOM), and iv) organic suspended solids or detritus (OSS). The total absorption coefficient is thus,

$$\alpha_{tot} = \alpha_{water} + \alpha_{Phyt} + \alpha_{MSS} + \alpha_{CDOM} + \alpha_{OSS} \quad (2.3)$$

The scattering and attenuation coefficients and the phase function (β) are also similarly summed.

The above IOPs are widely used in modeling the attenuation of spectral downwelling irradiance with depth, $E_d(\lambda,z)$. In the case of homogeneous water, attenuation is usually represented by the Beer-Lambert Law or

$$E_d(\lambda, z) = E_d(\lambda, 0)e^{-c\,z} \quad (2.4)$$

The equation is analogous, although not equal, to the attenuation of subsurface irradiance from diffuse solar light, where the beam attenuation coefficient is referred to as a diffuse attenuation coefficient

$$E_d(\lambda, z) = E_d(\lambda, 0)e^{-K_d z} \quad (2.5)$$

and K_d is the sum of specific coefficients for absorption and scattering due to organics and mineral particles as above (See for example Sathyendranath et al 1987; Bricaud et al 1986; Johnsen et al 1994; Babin and Stramski, 2005; Wozniak and Stramski 2004). K_d values generally range from less than 0.1 m^{-1} for clear lakes (Hargreaves, 2003; Morel et al., 2007) to 1.0 for turbid lakes. Coastal New England waters have typical $K_d(532)$ of ~ 0.2m^{-1} (Pe'eri et al., 2001, 2004) (Pers. Communication, Christopher Parrish, Oregon State University).

The above equation has important implications for ICESat2 since ATLAS 532 nm beams penetrate into the water column. The retrieval of the surface water height thus needs to account for 532 penetration. However, initial MABEL studies indicate that the mean water surface height correction may be small for inland water, on the order of several centimeters, due to fairly turbid water. Typical attenuation coefficients of several US lakes are shown in Table 2-1.

LAKE	k (m^{-1})	Secchi Depth (m)	Euphotic Zone (m)	Description
Crater Lake (OR)	0.06—0.12	25—45	>120	Clear, sky blue ultra-oligotrophic lake
Lake Tahoe (CA/NV)	0.12	40	90—136	As above but decreasing clarity since1960s due to watershed overdevelopment http://www.trg.ucdavis.edu
			Lake Superior	
Lake Superior (Blue water)	0.13	15—20	46—60	Ultra-oligotrophic; most oligotrophic of the Laurentian Great Lakes
Lake Superior (Green water near Duluth)	0.3	5—12	20—30	Western arm near Duluth and St. Louis River and harbor inputs
St. Louis River (Duluth-Superior Harbor)	4.21	0.7	>5	Brown (bog) stained from river plus high suspended sediments
Lake Michigan	0.19—0.24	?	19—31	Meso-oligotrophic
Lake Huron	0.1 — 0.5	?	25—31	Meso-oligotrophic
Lake Erie	0.2 — 1.2	2—10 (1970—1990) >10 (1993—1995)	12—26	Eutrophic (clarity improving recently due to zebra mussels)
Lake Ontario	0.15 — 1.2	?	12—29	Mesotrophic
Lake Baikal, Siberia	0.2	5—40	15—75	Oligotrophic
Grindstone Lake (Pine County, MN)	0.82	3—6	8—20	Mesotrophic, water is fairly stained or colored
Ice Lake (Itasca County, MN)	0.83	2—5	6—15	Mesotrophic
Lake Minnetonka (Hennepin County, MN)				
West Upper	0.78	1.4	3—5	Mesotrophic
Halsted Bay	2.9	0.5	<2	Eutrophic

Table 2-2 Typical values of attenuation coefficient for US lakes from (www.lakeaccess.org)

2.3 Lidar Remote Sensing Over Water

2.3.1 Airborne Lidar

The application of airborne scanning lidar over water including surface and subsurface targets is well documented (E.g. Churnside, 2014, Guenther, 1985). Much of the US interagency work is coordinated through the Joint Airborne Lidar Bathymetry Technical Center of Expertise (JALBTCX) supporting the US Army Corps of Engineers (USACE) and National Oceanic and Atmospheric Administration (NOAA) , the U.S. Naval Observatory (NAVO) and the U.S. Geological Survey (USGS). Mapping generally includes coincident 532 and 1064 nm lidar in conjunction with hyperspectral imagery. However, several systems that only employ 532 include the NASA/USGS EAARL, the more recent EAARL-B (Wright, 2014), and the Riegl VQ-820-G.

Although both 532 and 1064 nm light only reflects approximately 2% at the water surface due to Fresnel refraction, the 1064 nm wavelength absorbs nearly all the remaining 98% within the first meter, while the 532 nm wavelength both scatters and absorbs at depths to several tens of meters depending on water IOPs. The difference between 1064 and 532 backscatter thus facilitates identification of the water surface height, limited profiling of water depth optical properties associated with mineral and other particulate scattering, and also bottom topography.

The depth dependent lidar signal from airborne sensors has been described in terms of one expression that combines the instrument properties, the scattering properties of the water surface and subsurface attenuation (Churnside, 2014) or

$$S(z) = \frac{EAO(z)T_O T_S^2 \eta n v}{2(nH+z)^2} \beta(\pi, z) \exp[-2\int_0^z \alpha(z')\mathrm{d}z'] + S_B, \tag{2.6}$$

where the instrument properties include, the detector photocathode current *S(z)*, the transmitted pulse energy, *E*, the receiver area, *A*, the overlap function, *O* between the laser beam and the received field of view, the transmission of the receiver optics, T_O, the transmission through the water surface, T_S, the responsivity of the photodetector, η, the distance from the lidar to the surface, *H,* and the photocurrent due to background light, S_B. Water properties include the path length in water *z*, the refractive index of water, *n*, the speed of light in vacuum *v*, the volume scattering coefficient at a scattering angle of π radians β, and the wavelength dependent lidar attenuation coefficient, $\alpha = \alpha(\lambda)$. In homogeneous water, the return signal in Eqn (2.6) effectively reduces to

$$S(z) = C \frac{\exp(-2\alpha z)}{(nH+z)^2} \quad (2.7)$$

Where S(z) is the signal at depth z and C is a parameter that depends on geometry, wavelength and lidar characteristics (Churnside et al, 1998).

A schematic of the scattering and absorption processes resulting from a lidar beam impinging on the water surface is shown in Figure 2.7 (Guenther, 2000). After surface refraction, the approximately 98 % of the lidar beam that impinges the water surface penetrates into the subsurface where it scatters and absorbs, spreading out into a cone of increasing angle. Beam spreading from the original surface footprint occurs over 360 degrees and represents the greatest effect in the dissipation of the lidar beam. Depending on the depth and attenuation of the water column, a relatively small portion of light reaches the bottom, where it exhibits lambertian scattering back up through the water colum, where it is further attenuated, and further scattered at the water air interface. The bottom reflected energy, like the volume scattered energy, will be spread out over a much larger diameter than the incident beam. As a result, only small a fraction of both the volume scattered and bottom reflected energy returns to the receiver. However, in very shallow areas, the 532 nm beam can have nearly no surface return, with the dominant return coming from the bottom, especially in very clear water (Nayegandhi, 2014).

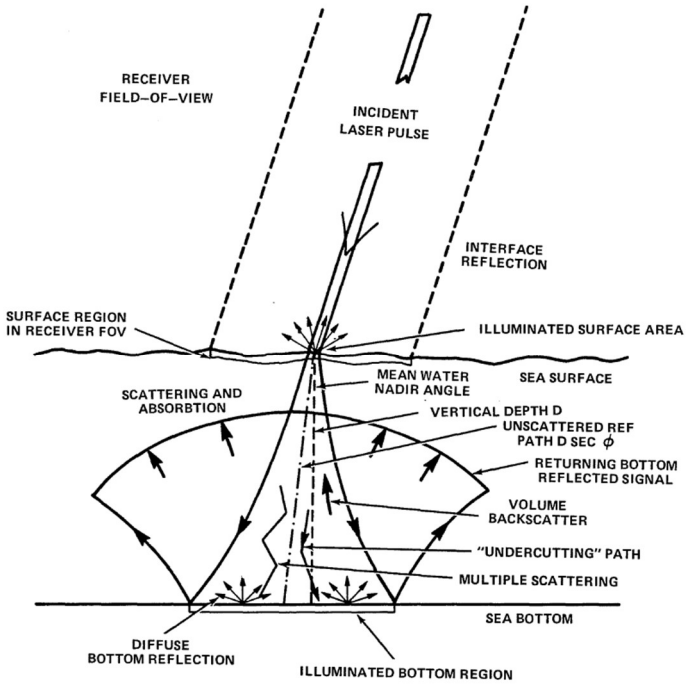

Figure 2-7 Sketch of process lidar subsurface backscattering processes in shallow water (from Guenther, 2000)

Once the laser beam has penetrated the surface, each photon may be scattered elastically or inelastically, or absorbed (Exton et al., 1983). Elastic scattering is primarily due to Mie scattering from suspended particles (Browell, 1977). Inelastic scattering is a result of either the Raman effect or fluorescence. Both processes result in energy being re-emitted at a different wavelength that was initially transmitted by the lidar. An example for the 532 wavelength is shown in Figure 2-8 below.

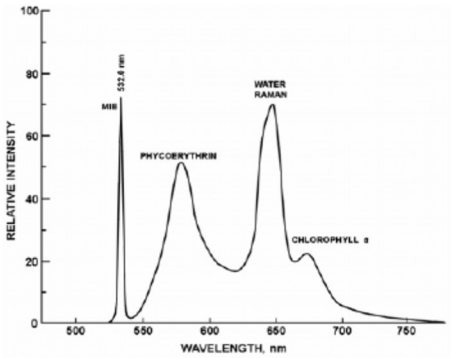

Figure 2-8 Backscattered spectra from natural water sample excited at 532 nm (based on Exton et al., 1983, and Pe'eri et al, 2007).

2.3.2 Satellite Lidar

Most satellite ranging studies over oceans have focused on wind speed analysis rather than subsurface bathymetry. Wind speed studies rely on modeling ocean surface backscatter from wave facets (E.g. Lancaster et al,2005; Menzies et al, Hu et al, 2008). Satellite based lidar water profiling over coasts have not been developed due to the high lidar power requirements, and also due to the lack of for 2D satellite scanning observations.

The specular reflectance of lidar and radar from the water surface has been investigated by Barrick (1968), Bufton et al (1983) and (others), including satellite-based studies (Menzies et al, 1998; Lancaster et al, 2005). Lancaster et al (2005) focused on ICESat GLAS reflectance of the ocean surface, although off- nadir pointing was not included. Menzies et al (1997) were the first to examine sea surface directional reflectance and wind speed using the LITE instrument aboard the space shuttle. Hu et al (2008) examined surface wind speed variability using NASA's Cloud-Aerosol Lidar with Orthogonal Polarization (CALIOP) Lidar backscatter data employing the Cox and Munk slope variance – wind speed relations.

The capability of satellite lidar to detect subsurface scattering has been examined by a number of investigators including (Jasinski et al, 2016; Lu et al, 2014; Churnside et al, 2013; Behrenfield et al, 2013; Barton and Jasinski, 2011) using CALIOP profiling and other high altitude lidar.

The feasibility of ICESat-2/ATLAS retrievals of inland water have been established in numerous airborne lidar engineering and science studies and the ICESat/GLAS mission, including lakes. The ICESat/GLAS instrument was a single beam analog sensor with an approximately 70 m footprint and along track spacing of about 180m. Inland water observations were successfully explored with accuracies in the cm to decimeter range, and its height products were used in a number of research and operational programs. The data were utilized in both lake and river studies (e.g. Harding and Jasinski, 2004, Birkett et al., 2010, Calmant et al., 2008, Zhang et al., 2011) that require both height and surface water slope. ICESat heights were also used to validate radar altimetry measurements from ENVISAT and OSTM in the absence of in situ gauge data.

Barton and Jasinski (2011) developed a formulation using CALIOP lidar to retrieve subsurface backscatter as the residual term in the total water backscatter equation. They incorporated the Hu et al (2008) surface specular reflectance that is wind and view angle dependent. The depth-

integrated attenuated backscatter (at wavelength λ, in nm) from the water surface viewed by the satellite was represented as a linear sum of surface and subsurface scattering. Results indicated the feasibility of using satellite lidar for observing both surface and subsurface reflectance characteristics in Case II coastal waters.

2.3.3 **The Multiple Altimeter Beam Experimental Lidar (MABEL)**

The Multiple Altimeter Beam Experimental Lidar (MABEL) was built as a high-altitude prototype of the ATLAS instrument (McGill *et al*. 2013) but possessing additional beams and flexibility to test variations in the ICESat-2 concept. In this capacity, it served several purposes including validation of ICESat models of instrument performance, evaluation of the photon counting system in the 532 nm band, providing experiment data over actual ICESat-2 targets, and development of retrieval algorithms of ICESat-2 data products. From 2012 through 2015, major flight experiments were conducted in Greenland, the east coast United States, the western US, and Alaska. In all these experiments, MABEL was flown aboard either the ER-2 or Proteus Aircraft, at 20 km or above 95% of the Earth's atmosphere. The high-altitude platform more realistically replicates the impact of clouds that ICESat-2 encounters, and that needs to be addressed in the retrieval algorithms. A summary comparison of the relevant ATLAS and MABEL instrument parameters is provided in Table 1-1. The configuration of MABEL beams is shown in Figure 2-9.

Figures 2-10 and 2-11 show typical results from MABEL flights over the Chesapeake Bay and the Atlantic Coast near Virginia Beach, respectively. The figures indicate raw MABEL geolocated photon clouds. Given that the MABEL instrument sampling design scales well with ATLAS, it has proven to be an important instrument for testing the ATL13 algorithm, described in Chapter 6 (Jasinski et al., 2016).

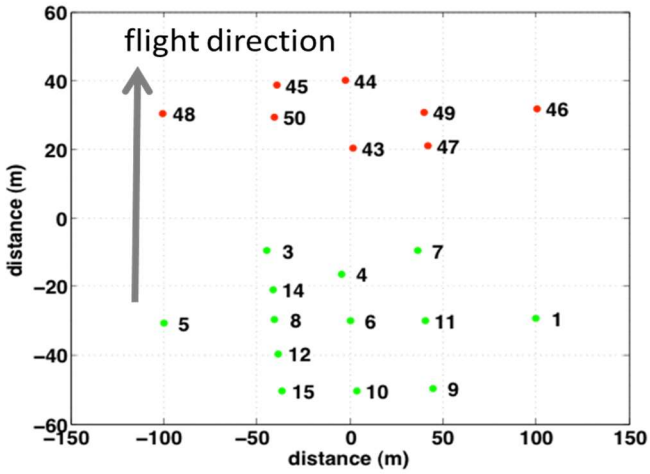

Figure 2-9 Configuration of MABEL beams.

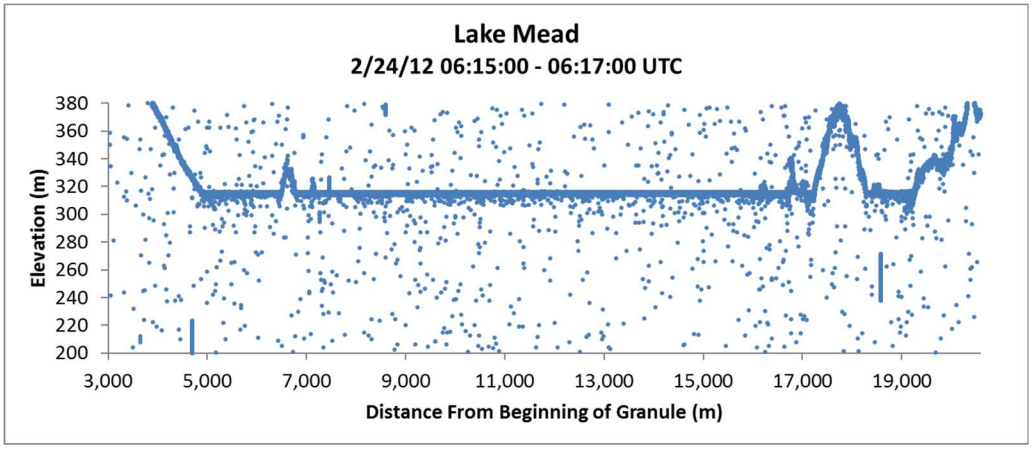

Figure 2-10 Photon cloud data from 2012 MABEL flight over Lake Mead (Jasinski et al., 2016).

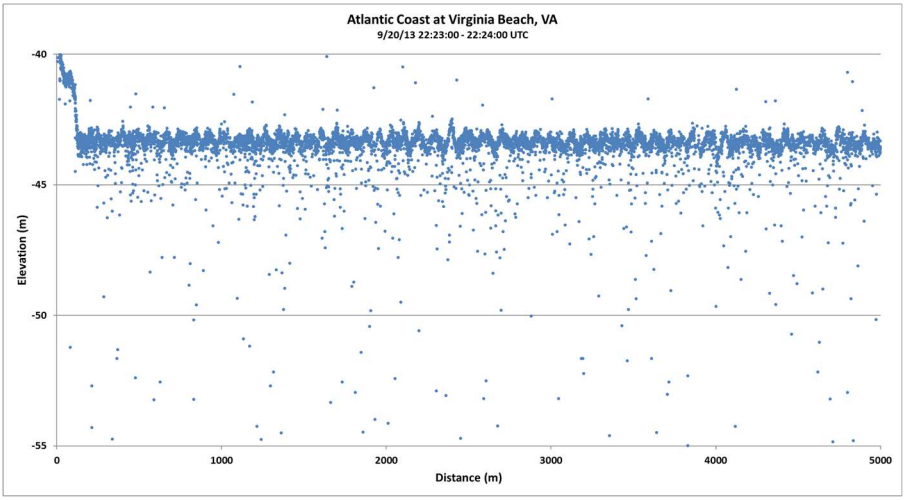

Figure 2-11 Photon cloud data from 2013 MABEL flight over Atlantic Coast near Virginia Beach (Jasinski et al., 2016).

3.0 INLAND WATER PRODUCTS

3.1 Conceptualization of ATLAS observed inland water reflectance

The photon returns reflected back to the satellite are conceptualized by the backscatter model shown in Figure 3.1. The photons received at the ATLAS sensor include backscatter from a number of atmospheric and water targets, including signal photons from ATLAS as well as noise photons from the sun and moon. The relative contribution of the sun will depend on solar zenith and azimuth angles, as compared to the ATLAS zenith and azimuth angles.

The depth-integrated attenuated backscatter γ^{tot} at 532 nm wavelength received by ATLAS from the water can be represented as a sum of backscatter components returning from the water, attenuated by the atmosphere, or mainly:

$$\gamma^{tot} = T_A\left[\gamma^{wA}(1-W) + \gamma^{fA}W + \gamma^{uA} + \gamma^{bA} + \gamma^{wS}(1-W) + \gamma^{fS}W + \gamma^{uS} + \gamma^{bS}\right] \quad (3.1)$$

where,

T_A = atmospheric 532 transmittance along the ATLAS look direction,
γ^{wA} = ATLAS specular backscatter from water surface back to receiver,
γ^{fA} = ATLAS Lambertian backscatter from foam on water surface back to receiver,
γ^{uA} = ATLAS volume backscatter from the water column back to receiver
γ^{bA} = ATLAS Lambertian backscatter light from the bottom
γ^{wS} = Sun specular backscatter from wavy water surface back to receiver,
γ^{fS} = Sun Lambertian backscatter from foam on water surface back to receiver,
γ^{uS} = Sun volume backscatter from the water column back to receiver
γ^{bS} = Sun Lambertian backscatter light from the bottom
W = fraction of foam covered water surface

Other possible components not listed in (3-1) include scattering from surface slicks, and scattering by spray in regions of high winds, solar background, lidar background, and dead count.

Since ATLAS photons are pulsed at 10kHz and subsequently received by the ATLAS detector, their time of travel and hence range can be determined. Solar photons, however, are generated in a continuous stream, so that individual ranges cannot be determined and are thus treated as background.

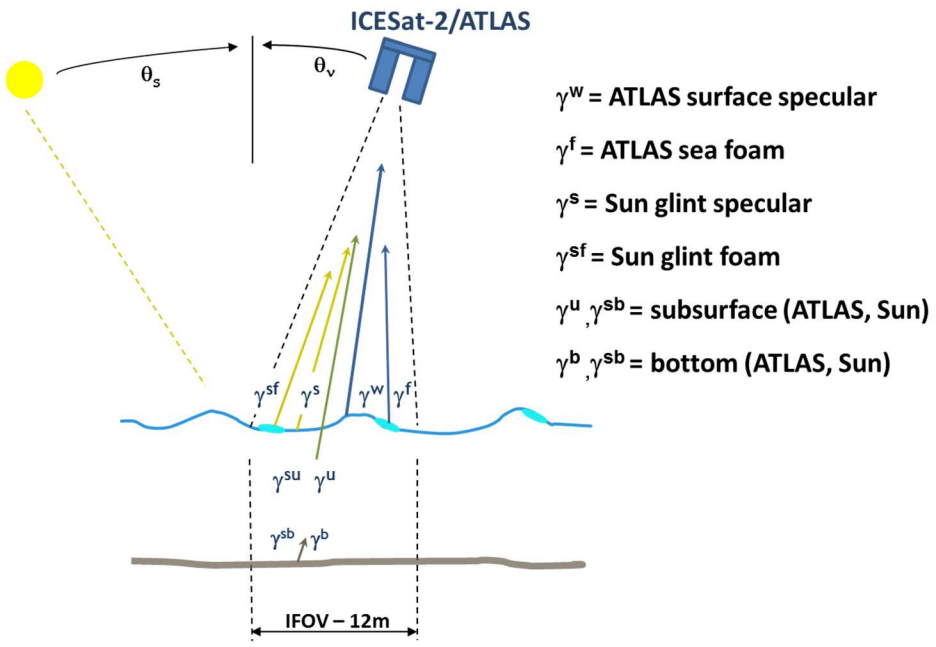

Figure 3-1 Components of the inland water height backscatter model, from Barton and Jasinski, 2011.

The relative magnitude of the backscatter components contributing to the total depth integrated backscatter equation (See Section 4.2) is computed for each L-signal photon segment (E.g. long segment, 1000 signal photon default) for both strong and weak beams. The main purpose is to understand the relative contribution of solar glint, solar foam scattering, and bottom scattering to the overall reflectance equation. The backscatter quantities include, for both ATLAS and Solar sources respectively, the specular backscatter from smooth water surface back to receiver (γ^{wA} , γ^{wS}) and the Lambertian backscatter from foam on water surface back to receiver (γ^{fA} , γ^{fS}). Also computed are the ATLAS volume backscatter from the water column back to receiver (γ^{uA}), and the total ATLAS plus solar Lambertian backscatter light from the bottom (γ^{bA}), and the fraction of foam covered water surface (W). The sum of the solar terms represents the principal contributions to the observed background count.

3.2 Conceptualization of ATLAS observed inland water altimetry

The analysis of the surface signal photons for each beam provides for each segment i) the vertical probability distribution of the height of the wave facets observed by ATLAS, including mean, standard deviation, and along track slope, ii) the distribution of the surface water height including mean, standard deviation, and skewness, iii) the distribution of volume scattering photons and the lidar beam attenuation coefficient, and iv) the identification of potential bottom signal if it exists.

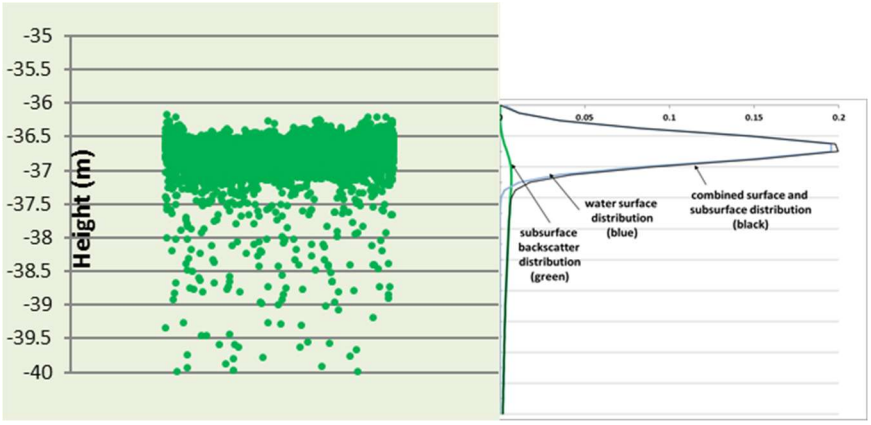

Figure 3-2 Conceptual interpretation of ATLAS vertical photon cloud histogram over inland water consisting of surface water photons and subsurface volume scattering photons.

3.3 Segment height statistics for strong and weak beams

For long signal photon segment (L_seg) lengths, the analysis provides along track mean height, slope, standard deviation, and attenuation coefficient as previously shown in Figure 1-1.

For each reported short segment length (S_seg1) of each strong and weak beam, analysis provides along track mean height, standard deviation, slope and attenuation coefficient, given sufficient data. The attenuation coefficient will be the same as that reported by the L_seg covering that short segment.

3.4 The ATL03 Inland Water Mask (Flag)

In order to facilitate processing of data over only land and near coastal regions that possess water bodies, three types of hydrologic masks are created: i) an ATL03 Inland Water Mask, ii) an ATL13 Regional Basin Mask, and iii) an ATL13 Inland Water Body Mask.

The Inland Water team (for ATL13) has worked with AT03 team to construct a gridded water mask of 0.1 km2 that flags whether or not one or more water bodies exist in that grid. Water bodies include lakes, reservoirs, impoundments and permafrost. The purpose of this fixed "Inland Water Mask", shown as the shaded regions in Fig 3-3 below, is one of efficiency. The implementation of ATL13 algorithm draws only on ICESat-2 observations that have been flagged as falling within an AT03 Inland Water Mask. The data base of the ATL03 Inland Water Mask does not identify the type of water body, only that one exists.

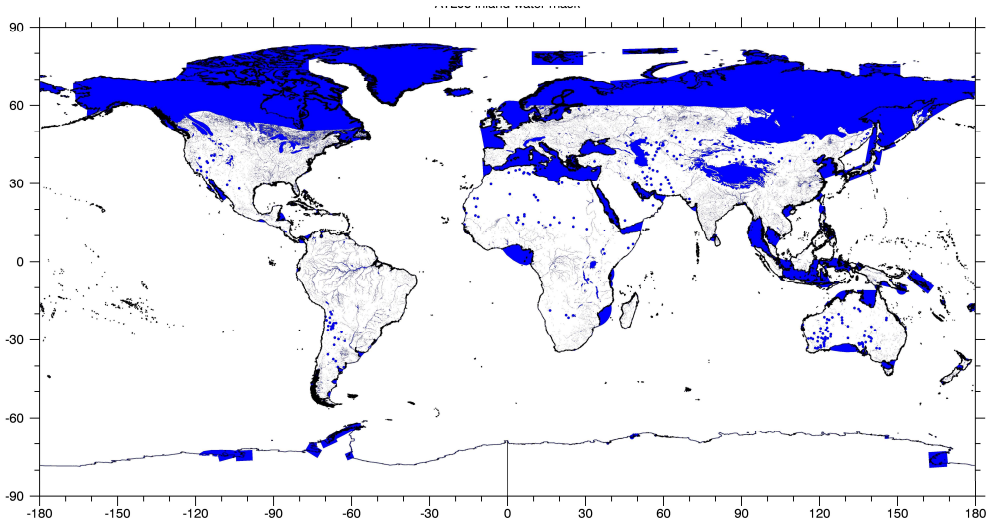

Figure 3-3 ATL03 Inland Water Mask (gridded, non-contiguous).

The ATL03 Inland Water Mask has been developed from a number of coastline and inland water databases including the Global Self-consistent, Hierarchical, High-resolution Geography (GSHHG) coastlines, various lake database shapefiles including ephemeral lakes, permafrost extent, and a custom set of shapes to close gaps in larger bays where not otherwise included. (ref: ATL03 ATBD)

3.5 ATL13 Regional Basin Mask (Shape File)

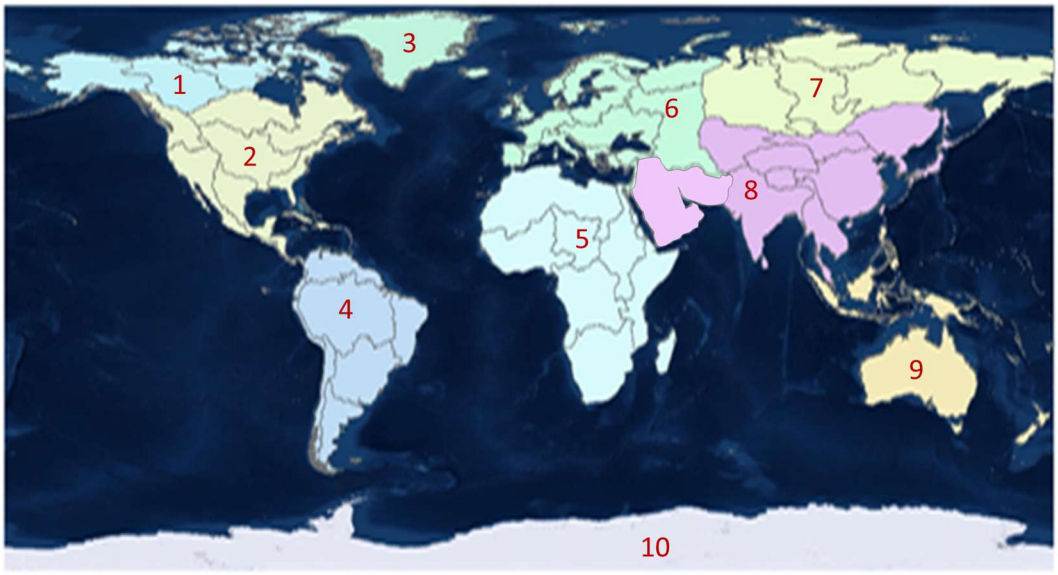

Figure 3-4 ATL13 Regional Basin Mask (Shape file).

The ATL13 Regional Basin Mask is used to organize the ATLAS data used for inland water calculations and hydrologic data products in a logical manner. It consists of polygons that represent principally the outline of entire large river basins and some adjacent intervening area. Each polygon contains all the lakes and rivers within that river basin. Archiving data products in this manner eliminates the problem of having to store ATLAS inland water data products of contiguous lake and rivers within different files. The regional basins are: 1= Northern North America; 2 = Southern North America; 3- Greenland; 4 = South America; 5 = Africa; 6 = Europe; 7 = Northern Asia; 8 = Southern Asia; 9 = Australia & Oceania; 10 = Antarctica.

3.6 ATL13 Inland Water Body Shape Mask (Shape file)

The ATL13 Inland Water Body Shape Mask facilitates identification of ICESat-2 crossings over individual water bodies. It delineates the shape and spatial distribution of contiguous individual water bodies. These include a composite of lakes, reservoirs, rivers, and transitional waters including estuaries and bays, and near shore coastal waters assembled by the inland water team for use in the ATL13 algorithm. An ATL13 Inland Water Body Shape Mask is employed as a

shape-file (E.g. HydroLAKES, Lehner and Messager, 2016; Global River Width from Landsat (GRWL) (Allen and Pavelsky, 2018); Named Marine Water Bodies, ESRI), unlike the ATL03 flag above which is a gridded product. The ATL13 Mask consists of polygons, each representing either an entire single lake or reservoir, 7-km wide coast segment, bay, or river segment including its tributaries. The ATL13 Inland Water Body Shape Mask includes an approximately 100m buffer extended over the land so that the land/water interface is identified.

An example of what the Water Body Mask looks like is shown in Figure 3-7 below for Alaska. Each lake is identified by number, lat/long, and local name if available.

Figure 3-5 Example of ATL13 Inland Water Body Shape Mask (contiguous lakes)

(from Lehner and Messager, 2016)

It is estimated that the multi-beam ATL13 ICESat-2 coverage contains potentially over 1.4 million water bodies, allowing the overpass of about 650 lakes ≥ 100km2, of which 50% are in Canada, and 25% in Eurasia. For lakes ≥ 10km2, the estimate is about 19,300 lakes.With 100 photon along-track aggregation there is the potential to record heights of the more numerous smaller impoundments (> 1-5 km2) which number in tens of thousands. Height accuracy will depend on aggregation level and water state but is expected to be about 10cm for the strong beam.

4.0 ALGORITHM THEORY

4.1 Overall Approach

ATLAS observations provide information on both the altimetry and the backscatter of the water surface and subsurface. Of principal interest for ATL13 is the altimetry that will provide information on along track height statistics. However, knowledge of backscatter also will contribute to understanding the water apparent reflectance, slope distribution, wind speed and subsurface backscatter attenuation.

The overall goal is to estimate short (~100 photon) segments of mean height for each ATLAS beam that crosses a water body in the along track direction. In general, although the far majority of the returned photons are specular photons returned from the water surface, up to several percent are returned as part of the subsurface volume backscatter. Thus, prior to estimating the short segments height statistics, it is necessary to first analyze estimate the volume scattering parameters which require long segments of 1 to 3 km that provide the sufficient number of subsurface photons.

The retrieval of the inland water height algorithm for ATL13 thus involves a combination of physical and statistical modeling of key physical processes related to open water surface dynamics and light propagation, as outlined in Chapters 2 and 3. Analysis primarily uses data from ATLAS ATL03 products, and also from external sources including meteorological data. The key steps include i) identifying the intersection of a contiguous water body and beginning and ending water edges of individual ICESat2 beam, ii) modeling the reflectance components that contribute to the integrated signal exiting the water surface toward the receiver, iii) analyzing models of the surface water height statistical distributions, subsurface volume scattering, and their relation to the distribution of the signal photons that emanate from water surface facets and back to the receiver, iv) extraction of the true representation of water reflectance and height by removing background photons, v) deconvolving of the ATLAS observations with its instrument response function, and vi) reporting the statistics of along track data products including principally the surface water height, but also the subsurface attenuation, significant wave height, and mean maximum water surface slope and azimuth from two adjacent strong beams. An evaluation of the accuracy and quality of the measurement is made.

The overall approach is to choose algorithm components that i) are commensurate with the range of scales of the inland water body product, and ii) that allow for a robust operational computation of surface height over the vast range, types and conditions of inland water bodies that ICESat-2 encounters during its lifetime.

The essential theoretical basis to implement the above strategy is briefly reviewed below.

4.2 Satellite Inland Water Backscatter Model

4.2.1 Water surface specular model

Water surface specular reflection is the largest component to the backscatter. Since specular returns reflect back toward the lidar receiver only if the wave facet surface slope equals the off-pointing angle, reflection models are based on the distribution of wave facets. Both Gaussian and near Gaussian distributions have been employed. Specular reflection decreases with increasing wave size and is therefore greatest in calm waters.

ATL13 employs either i) the Gaussian or the Gram-Charlier (Cox and Munk, 1954) wave facet slope model for the water surface distribution, and ii) the Cox and Monk type wind variance model shown in Eqn 2-2. Various combinations of these models have been used by previous investigators (E.g. Hu *et al.* 2008, Platt, 1973; Menzies *et al, 1998*, Tratt *et al, 2002*, Lancaster et al, 2005) that depend, in some cases, on the source of the input data. For instance, in analysis of wind speed fields using CALIOP observations using AMSR-E wind fields, Hu et al (2008) assumed a Gaussian surface height distribution for specular reflectance or

$$\gamma_\lambda^w = \frac{\rho_\lambda}{4\,\pi\,\sigma_s^2\,cos^4\theta}\,exp\left[\frac{-tan^2\theta}{2\sigma_s^2}\right] \tag{4.1}$$

where ρ_λ is the Fresnel specular reflection coefficient ($\rho_{532} \approx 0.0209$), σ_s^2 is the wave slope variance (or mean square slope, MSS), and θ is the zenith angle of the sensor. The Hu *et al* (2008) composite model for the wave slope variance, modified at the upper and lower ends of the wind speed spectrum from that of Cox and Munk, is

$$\sigma_s^2 = \begin{cases} U < 7m/s & 0.0146\sqrt{U} \\ 7 \le U < 13.3\,m/s & 0.003 + 0.00512\,U \\ U \ge 13.3\,m/s & 0.138\log_{10}U - 0.084 \end{cases} \tag{4.2}$$

where U is wind speed.

4.2.2 Water surface foam model

The scattering of the lidar from whitecaps and foam streaks on the water surface can be significant, although this component is mainly a factor at wind speeds higher than about 10 m/s. At this speed, the magnitude of foam scattering approaches the volume scattering of low

turbidity natural waters. Moore *et al.* (2000) modeled the reflectance of foam as a function of wind speed. In this model the reflectance of the foam is expressed as an "additional" contribution to reflectance, representing the increased reflectance of the ocean surface due to the foam. At 532 nm, the foam backscatter is modeled as a Lambertian process or,

$$\gamma^{fA} = W\gamma^{wA} + 3.14 \times 10^{-6} U^{2.55} \frac{\cos\theta}{\pi} \tag{4.3}$$

from foam covering a fractional area, *W*, described by Callaghan and White (2009) or

$$W = \begin{cases} U < 3.70 & 0 \\ 3.70 \leq U < 10.1874 & 3.18 \times 10^{-5}(U - 3.70)^3 \\ U \geq 10.1874 & 4.82 \times 10^{-6}(U + 1.98)^3 \end{cases} \tag{4.4}$$

4.2.3 **Volume scattering model**

Models of subsurface scattering applied to airborne lidar have been developed (e.g. Gordon, 1982; and Phillips and Koerber, 1984) in terms of the water optical properties including volume backscatter and attenuation coefficients. These may be applicable to ATLAS, however, they need to be tested on MABEL data. Because many of the atmospheric and instrument parameters are not precisely known, the subsurface backscatter is modeled similar to Equation (2.5)

$$\gamma^{uA}(d) = \rho_s(d) = \beta * \alpha * c_l * \exp(-\alpha * d) \tag{4.5}$$

where α is the attenuation coefficient, β is coefficient that includes both instrument and backscatter magnitude, c_l is a correction for light speed (assumed =1/1.3) and d is depth.

4.2.4 **Bottom reflectance**

Bottom reflectance is treated as a Lambertian surface.

4.2.5 Relative magnitude of anticipated returns

The relative magnitudes of typical ATLAS backscatter terms for the strong beam is shown in Figure 4-1 below following the approach by Barton and Jasinski (2011). Results are presented as a function of wind speed. The typical scenario shown in Figure 4-2 represents an ATLAS strong beam and 0.3 deg off Nadir view, and a solar zenith angle of 30 deg. Results exhibit a strong dependency on wind speed. For instance, for wind speeds greater than about 7 m/s, the contribution from sunglint and sun foam are over an order of magnitude smaller than their ATLAS counterpart. However, the sunglint contribution is about the same magnitude as ATLAS foam scattering for wind speeds greater than about 10 m/s.

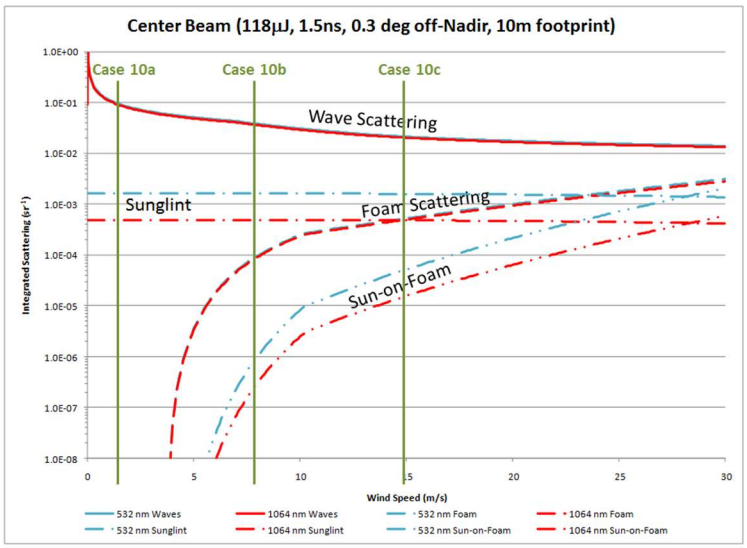

***Figure 4-1 Relative contribution of water backscatter** terms (Barton and Jasinski, 2011).*

4.2.6 Atmosphere and Meteorology input

The specular water surface and foam backscatter models requires wind speed and atmospheric transmittance, *T*, including Raleigh, cloud, and aerosol effects. When *T* or cloud cover are known, wind speed can theoretically be estimated using Hu et al.'s equation in 4.1. Otherwise, wind speed is obtained externally from ATL03 through modeled sources, such as the European Centre for Medium-Range Weather Forecast (ECMWF) model. Cloud cover may be available from GOES imagery depending on location.

4.3 Water surface height model

4.3.1 Photons contributing to the water surface height

The signal photons contributing to the water surface height distribution are those associated with the ATLAS related scattering terms in Equation 4.1. The signal photons not associated with the surface height need to be identified and, in some cases, removed. These generally appear as somewhat uniformly distributed background photons in the vertical profile, both above and below surface. Their source primarily consists of the solar background, although some ATLAS dark count background also may exist. Background is obtained from the ATL03 data product. Removing background effects in ATL13 is implemented by subtracting off the uniform amount from the surface height histogram, leaving only the terms $\gamma^{wA}(1-W)+\gamma^{fA}W+\gamma^{uA}$.

For a given water body crossing, analyses are executed for each transect, where a transect is a portion of the ICESat-2 crossing uninterrupted by land such as islands, peninsulas or meanders. Transects are defined by the mask and are buffered based on water body type. The transect is tested to determine if anomalous short segment(s) exist at either the beginning and/or end of the transect.

4.3.2 Estimation of Background and Signal to Background Noise Ratio

An expression of the vertical profile of MABEL's observable subsurface backscattered signal photons is required to separate the surface water and subsurface photons, and to understand the depth of penetration. This is estimated based either on i) classified ATL03 photons or ii) formulated as the ratio of the depth dependent signal photon density to mean background density, SBR(d), written (after Schroeder 1999; Jasinski et al., 2016).

4.3.2.1 Estimation of background count based on classified photons

ATL13 utilizes the signal classification designations from ATL03 to compute background. The ATL03 computes background counts obtained over a 50-shot time interval (200 Hz), reduced by the signal photons and potential TEP photons, over a variable altimetric range window height that is reduced by the signal photon span height. The ATL13 background density (counts/m) is computed as:

Bckgrd_Dnsty_50sht = ***bckgrd_counts_reduced/bckgrd_int_height_reduced***. (4.6a)

The background density per 50 shots over each ATL13 5cm histogram bin is thus

Bckgrd_Dnsty_50sht_5cm = Bckgrd_Dnsty * 0.05. (counts). (4.6b)

Bckgrd_Dnsty_50sht_5cm is the same for each bin but can change along track.

The background density over an ATL13 short segment must account for the length of the segment and thus the sum of each 50-shot reporting within that segment.

$$\text{Bckgrd\_Dnsty\_50sht\_5cm\_Sseg} = \Sigma_{i=1,\ N\_50sht\_Sseg}\ \text{Bckgrd\_Dnsty\_50sht\_5cm}_i. \quad \text{(counts)} \quad (4.6c)$$

Where "i" is the index of 50-shot (200 Hz) reportings in the short segment, or

N_50sht_Sseg = Length_short seg/(G_spd/200) (unitless) (4.6d)

where G_spd is obtained from ATL03 (nominally 7000 m/s). If $\text{Bckgrd\_Dnsty\_50sht\_5cm}_i$ only partially overlaps the leading or trailing ends of the short segment, only include the respective fractional overlap of those background photons. Report the background density for each short segment in terms of flags based on threshold values.

4.3.2.2 Estimation of ATL13 signal to noise ratio

The signal to noise ratio is expressed

$$SBR(d) = \frac{\rho_L(d)}{\rho_{SB} + \rho_{LB} + \rho_{DC}} \quad (4.7a)$$

where $\rho_L(d)$ equals the observed lidar signal photon density (m^{-2}) as a function of depth, d, and the denominator represents the sum of the mean of all background noise densities (m^{-2}) including solar background, ρ_{SB}, lidar background, ρ_{LB}, and dead count, ρ_{DC}. Mean background density, constant throughout the vertical column, was computed as the mean number of non-signal photon counts in the atmosphere above the water surface, per meter depth per meter transect (m^{-2}). During daytime, the background consists mostly of solar backscatter. At night, the background density drops significantly and is primarily due to lidar backscatter.

Because both the total observed return and the mean background can be computed directly from the observed vertical profile, and because the background can range over several orders of magnitude, Equation 4.6 is more conveniently rewritten as

$$LSBR(d) = \ Log_{10}\left[\frac{\rho_L(d) + \rho_{SB} + \rho_{LB} + \rho_{DC}}{\rho_{SB} + \rho_{LB} + \rho_{DC}} - 1\right] \quad (4.7b)$$

where the numerator in the brackets represents the total return observed by MABEL including both signal and background photons. Prior to computing *LSBR(d),* a vertical histogram of the total return is created at 0.05 m bin increments using all water photons observed along flight path. The mean background in the denominator is estimated from observed atmospheric photons. *LSBR(d)* is computed and smoothed employing a 0.5 to 1.0 m moving average as necessary depending on the specific site.

A threshold value where LSBR(d) = -1 or $LSBR_{-1}$ represents where the SBR =0.1 (Alternately, $LSBR_0$ represents where the SBR =1).

Although computed successfully using MABEL observations (Jasinski et al., 2016) the robustness of the LSBR is currently under evaluation. A default value of 5 -10 m can be used as $LSBR_{-1}$ over open water of most lakes.

4.3.3 **Estimation of water surface height and slope variance**

A Gaussian distribution of water surface height is assumed, defended scientifically (E.g. Mobley, 1994) and based on the Central Limit Argument. Use of the Gaussian may also be the most practical assumption given the operational nature of the ATL13 data product, and it having to compute, globally, a wide range of lake types, sizes and wind speed conditions. Further, there is some justification for the Gaussian water based on MABEL analysis and smaller heights compared to open ocean. Thus, the Gaussian distribution may be more suitable for small water bodies (< 5-50 km), where it can be assumed fetch and wave height is small.

Recent analysis of MABEL flights over inland water targets appear to support the Gaussian assumption. Examples of this approach applied to MABEL data showed very good accuracy, as shown in Section 2.4.3. For large water bodies, where wave heights can be large especially for winds > 7m/s, a greater number of signal photons from larger segment lengths allows better characterization of the surface height distribution including its higher moments. Analysis thus employs empirical relations among wave slope variance, water height variance, significant wave height, significant slope and wind speed.

4.3.4 **Estimation of water surface slope variance**

A key step in retrieving wave reflectance properties is knowledge of the mean square slope of the wave facets. The mean square slope (MSS) can be estimated from the elevation spectrum, or the Fourier transform of the autocovariance function of the surface height. The MSS in the omnidirectional context is expressed (E.g. Elfouhaily et al, 1998)

$$MSS = \int_0^\infty k^2 S(k) dk$$

where k is wavenumber and $k^2S(k)$ is the omnidirectional slope spectrum.

A simpler approach is employed in ATL13, is estimating MSS based on histograming the photon cloud. Literature review indicates there are only few studies directly relating the distribution of water height to water slope including non-Gaussian (Longuet-Higgins, 1963; Tayfun, 1980; Huang et al, 1984). There is unfortunately little available literature on the correlation between wave slope and wave height distribution.

However, an estimate of the water surface variance can be made using recently published results by Kay et al (2011). Drawing on results from other investigators (Apel, 1994; Cox and Munk, 1954; Elfouhaily et al, 1997; Zaneveld, 2011), they pointed out that the mean square slope is proportional to wind speed, while the height standard deviation is proportional to the square of wind speed. Their graphical results are shown below in Figure 4-2. They also indicate very good agreement with the Cox and Munk (1954) wave slope - wind speed relation.

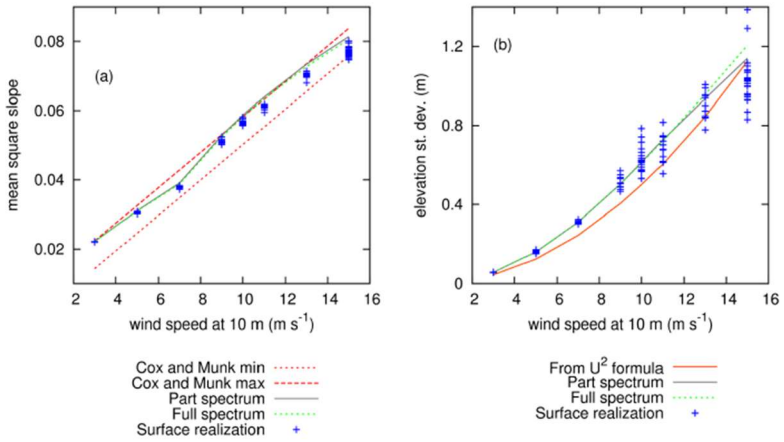

Figure 4-2. Wind speed dependence of mean square slope (left) and height standard deviation (right) (After Kay et al, 2011).

By combining the above two figures, a relationship is developed between the mean square slope (MSS) and the water height standard deviation when wind is present. For this, use the σ_h height wind speed relation (Fig 4-2 left., summarized by Kay et al, 2009) or

$$\sigma_h = 0.005 * U^2 \tag{4.8}$$

in conjunction with the MSS-wind speed relations by Hu et al (2008) in Equation 4.2 (or the Cox and Munk (1954) relations in equation 2.2) which lead to Figure 4-3 below.

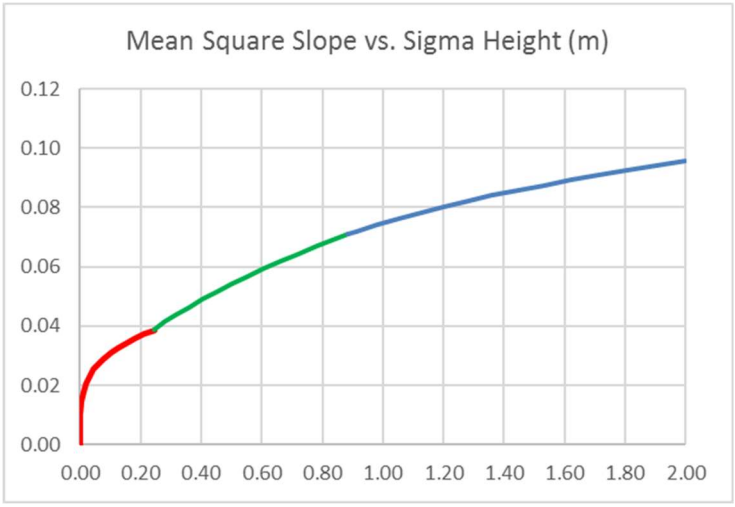

Figure 4-3 Relationship between MSS (or σ_s^2) and σ_h derived by combining Eqn. 4.8 from Kay et al (2011) with Eqn. 4.2 from Hu et al (2008), as shown in Eqn. 4.15. Colors represent different wind speed ranges.

Results show good consistency with analysis by Hwang et al, 2009, shown in Figure 4-4 below.

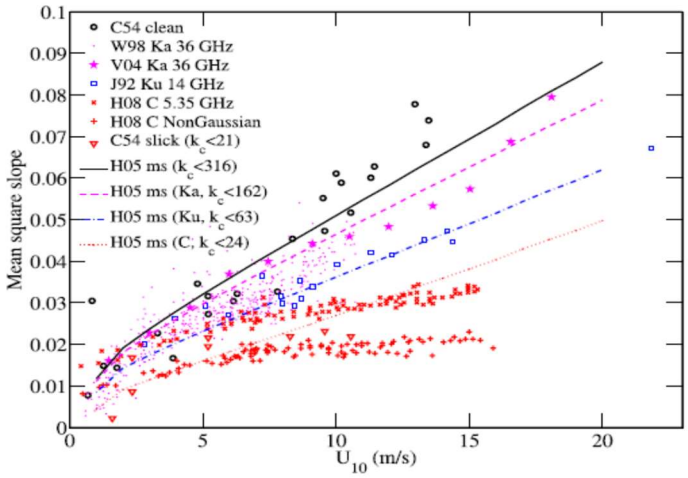

Figure 4-4 Filtered MSS as a function of wind speed based on measurements of airborne radars with different frequencies. [Jackson et al., 1992; Walsh et al., 1998; Vandemark et al., 2004; Hauser et al., 2008] and sun glitter analysis [Cox and Munk, 1954]. The smooth curves are the corresponding mss obtained from integration of the wave number spectral model (mixed sea condition) of Hwang [2005] with the upper cutoff wave number defined by Jackson et al. [1992]. J92, Jackson et al. [1992]; W98,Walsh et al. [1998]; V04, Vandemark et al. [2004]; H08, Hauser et al. [2008]; C05, Cox and Munk [1954]; H05,Hwang [2005]. (From Hwang, 2009).

When wind is not present, residual waves exist as swells. In this case, the relation between wave height and wave slope variance are determined from the observations.

4.4 Instrument response function (transmitted pulse shape)

All the photons within a given pulse are assigned the same time of departure. Since the instrument response function may extend over one or two thousand mm (See MABEL response function in Figure 4-5 below), the observed ATLAS signal photons' return time from the surface facet and foam height distribution represent an integration of all the photons from that pulse that may have slightly different start times depending on their position within the pulse. Consequently, a technique to deconvolve the distribution of the ensemble of surface signal photons from the instrument response distribution needs to be implemented.

A critical step in the surface water height retrieval algorithm is the deconvolution of the instrument transmitted response function (or histogram) from the observed histogram, in order to extract the actual water response histogram. Experience with MABEL indicates that the lidar pulse can be spread out over 2500 mm. See Figure 4-5 below obtained from the ICESat-2 Project Office. This long response function affects the observations by broadening the distribution of the returns, thereby distorting the true pdf of the combined surface height, volume scattering, and bottom reflected signal photons.

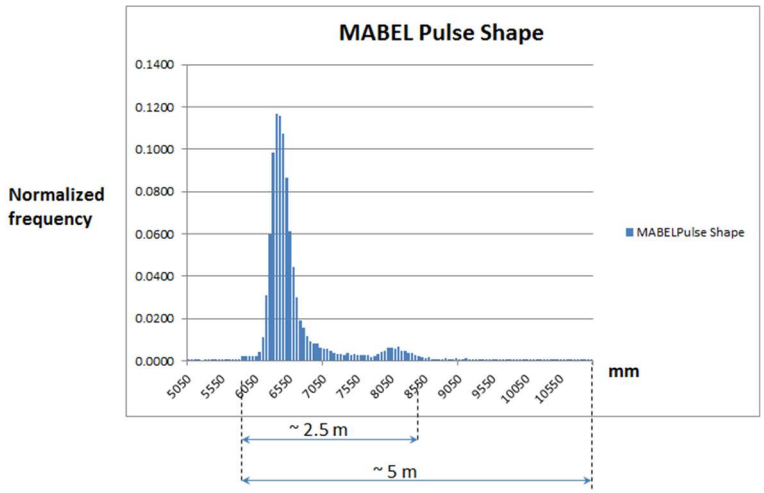

Figure 4-5 MABEL response function (from B. Cook NASA, 2012)

Figure 4-5 exhibits the typical histogram of the MABEL instrument in 5 mm bins ranging from 6000 to 8550 mm. The overall shape indicates a half-width, half max width of about 500 mm with after pulse peak about 2 m to the right. Although small, this tail must be considered in the full deconvolution order to improve retrieval accuracy and to fully understand the volume scattering effect which can be of the same magnitude as the tail.

4.5 Deconvolution of instrument response from lidar returns

4.5.1 Constrained Deconvolution Method

The Impulse Response Functions (IRF) of prototype photon counting sensors such as MABEL and SIMPL have shown to exhibit much variability, especially with regard to the existence of an

afterpulse with varying magnitude. Further since all photons pulsed are assigned the same time of departure, the true vertical distribution of observed photons can only be determined through a deconvolution of the observed IRF functions. The impact of the instrument response function thus needs to be removed in order to determine the true surface and subsurface distribution.

The height of the ATLAS signal photons represents the convolution of the instrument transmit pulse, and the water surface response. Thus, the true water surface response can only be obtained by deconvolving the instrument and surface response, given knowledge of the integrated observations.

This can be achieved using various parametric and non-parametric methods. However, experience based on MABEL analysis over several inland water bodies using non-parametric approaches, including spectral analysis and matrix inversion, indicates these approaches may not be robust for smaller inland water bodies. This is thought to be a result of the relatively small number of signal photons (several hundred) available to effectively compute at least a somewhat smooth histogram required for inversion.

Based on the above experience, a parametric, "Constrained Deconvolution" approach has been developed for ICESat-2 ATLAS measurements over inland water. The constrained deconvolution approach requires an assumption of an *a priori* functional form of the individual components of inland water backscatter. **It therefore solves the deconvolution problem while at the same time estimating the parameters of the model.**

A standard deconvolution integral is assumed for a linear system with finite time steps. Assigning the probability density function (pdf) of the instrument response function as x(t), and the actual or true unit vertical distribution of the water signal photons per unit pulse as h(t), then the integrated pdf of all signal photons returned to the receiver from the entire instrument response function, y(t), can be written as the convolution of x(t) and h(t). In continuous form,

$$y(t) = \int_0^t h(\tau)x(t-\tau)d\tau \qquad (4.9)$$

In discrete form, (4.9) can be expressed

$$y_j = \Sigma\, h_{i-j}\, x_i \qquad (4.10)$$

i = the number of instrument pulse bins and j is the number of output height bins. The y_j represents the histogram of the observed water photons for a given segment length, x_i is the lidar pulse histogram (IRF) measured over i bins. Finally, h_{i-j} represents the actual or true unit water surface response of the water, before bias correction.

4.5.2 Solution Approach

The solution to (4.10) is obtained by first assuming a functional form for the actual or unit water column h(t) with unknown parameters. The h(t) and x(t) are then convolved over a range of model parameters until a best fit of the model with the histogram of the observed signal photons is achieved. Thus, the model parameters of the water column including the true water surface height distribution, and the subsurface distribution, are resolved together within the deconvolution scheme.

A key element in the implementation is that each bin (5 cm width) of the IRF is convolved with the model. This is shown in Figure 4-6 for the particular MABEL response function during a 2012 flight over the Chesapeake Bay.

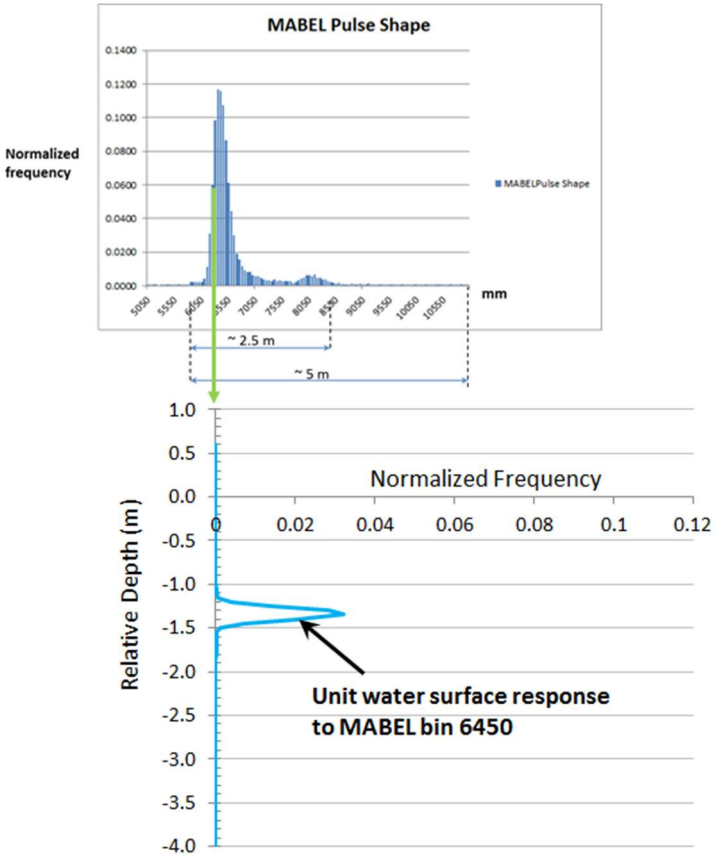

Figure 4-6 Constrained Deconvolution Method- Unit water surface response for one 5cm MABEL bin, arbitrarily selected as 6450 mm.

In the example, a Gaussian water surface height distribution is assumed with an exponential subsurface decay. Figure 4-6 shows MABEL bin 6450, with a normalized frequency of 0.0600, convolved with the model and an initial set of assumed parameters, resulting in a unit water response associated with that bin. Figure 4-7 shows the full convolution of all MABEL bins which are then summed and compared to the original MABEL observation. The optimal solution occurs when the convolved model best fits the observed data. The best fit analysis that partitions the subsurface and surface deconvolution and based on estimation of the standard error allows a better fit of the tails.

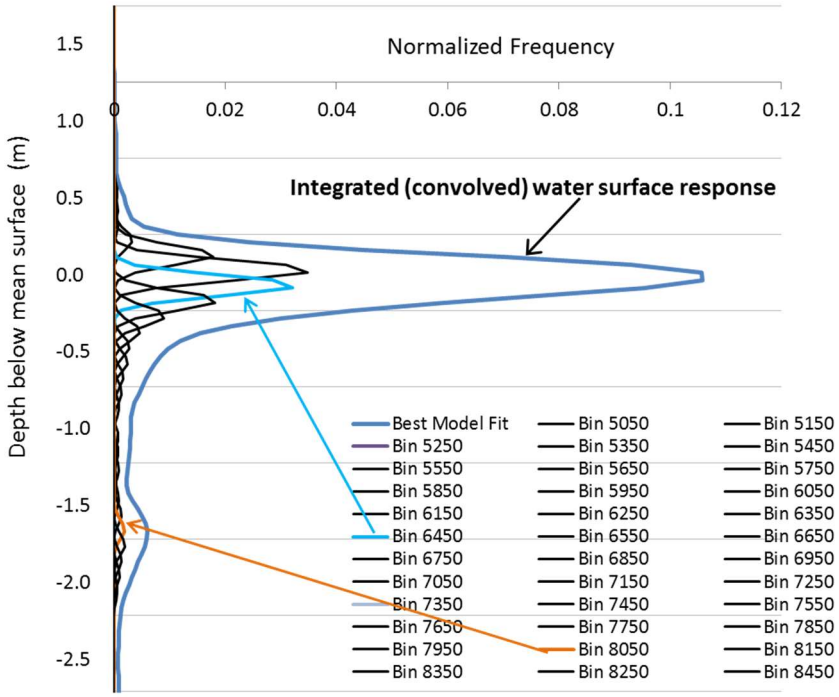

Figure 4-7 Constrained Deconvolution Method – Integrated response to all MABEL bins.

4.5.3 **Deconvolution of subsurface backscatter profile**

The water histogram contains four parameters: the mean (μ) and standard deviation (σ_h) of the unit Gaussian water surface, and the β and α of the subsurface exponential. Because of this, the deconvolution is solved separately, first for the subsurface profile and then for the surface profile. Identify and exclude bins associated with non-exponential anomalies and the water body bottom prior to computing subsurface profile, as described in section 4.5.5.5.

For the subsurface profile, the amplitude parameter, β**,** and α, using Eqn 4.6 or

$$y\_sub_j = \sum_{i=1}^{i=j} \{\beta * \alpha * \mathrm{cl} * \exp(-\alpha d)\}_{j-i+1} * X\_IRF_i * bin\_size \quad (4.11)$$

where X_IRF_i is the discrete IRF, α is the attenuation coefficient, β is coefficient that includes both instrument and backscatter magnitude, c_l is a correction for light speed (assumed =1/1.3) and d is depth.

The solution to fitting β and α is achieved over the range of minus 3-sigma below the mode of the detrended water surface (upper limit) to minus 3-sigma of the mean of the subsurface profile or -10m, whichever is shallower. The implemented solution is to minimize the error difference between integrated model and the ATLAS histograms, or

$$\min \ Err = \Sigma(y\_sub_j - y\_obs_j) \quad (4.11b)$$

However, other approaches (E.g. Method of Moments can be used to minimize the difference between the means and standard deviations of the integrated model and the observed (ATLAS) histogram.

4.5.4 **Deconvolution of surface water profile**

Once β and α are estimated, μ and σ_h are estimated within the convolution over the unit profile in 4.12 below. The β and α already computed above are held constant.

$$y\_tot_j = \sum_{i=1}^{i=j} \left(\left\{ \frac{1}{\sqrt{2\pi\sigma_h^2}} \exp\left(\frac{-(d-\mu)^2}{2\sigma_h^2} \right) \right\} + \left\{ 0.5 * \left[1 + \operatorname{erf}\left(\frac{d-\mu}{\sigma_h \sqrt{2}} \right) \right] * \beta * \alpha * \mathrm{cl} * \exp(-\alpha d) \right\}_{j-i+1} \right) * bin\_size \quad (4.12)$$

The solution is achieved by iteration over μ and σ_h until the difference between the integrated model and the ATLAS histograms are minimized, similar to that described in 4.5.3 above. The solution is fit over the upper 80% of the integrated Gaussian height.

Results include the mean and standard deviation of surface height of that segment of surface photons analyzed, reported at the center of the segment, together with the lidar attenuation coefficient. Mean surface height is determined as the mean of the deconvolved surface Gaussian distribution.

The solution trades off the simplicity of a non-parametric approach to deconvolution, for a highly robust solution that is more practical given the global domain of all the lakes, rivers and other water bodies that ICESat-2 traverses.

For the MABEL cases tested from 2012-2014 during the development of this ATL13 ATBD, the results provide a generally robust solution with very good comparison with observed data as shown in Figures 6-4, 6-7, and 6-9.

4.5.5 **Implementation of deconvolution**

4.5.5.1 Identification of water signal photons.

Photons are identified through a process of histogramming the vertical profile of all photons over a water body detected within the range of +20m to -40 m of the water surface. Short segment lengths are defined on the basis of 100 photons that are classified in ATL03 as signal photons. The coarse water surface is identified by computing the mode of each short segment within a group of three long segments. All photons within about 1.5 m+/- of the mode are selected for further analysis.

4.5.5.2 Detrend observed data.

Observed data are detrended prior to deconvolution. Detrending is achieved on a long-segment basis (1000 signal photons or 10 short segments) on the basis of fitting a linear line through all the photon data within +/- 1.5 meters of the coarse water surface. Once identified, the photon data within the short segment are trimmed to include only the range +10m (above) the to -20m (below) the zero-mean water surface. Histograms of each long segment are created at 5 cm bin resolution.

4.5.5.3 Remove background from observed data.

Once histogrammed, the background density is subtracted off each 5 cm bin rectangle. Calculation of the background density is described in Section 4.3.2.1. The value is the same for each bin. If the bin rectangle value after subtracting is less than zero, assume the value is zero.

4.5.5.4 Alignment of IRF and observed histograms.

During deconvolution, it is critical that the beginnings of the IRF, the observed histogram, and the integrated histogram (convolved profile) all begin at the same bin, near or slightly above, the very top of the observed water surface. The IRF is resampled to 5 cm bins and normalized to 1.0. The beginning of the IRF is defined as $3x\sigma_{h\_IRF}$ above the mean (to the left) of the best fit Gaussian to the IRF. The end of the IRF is defined as $8x\sigma_{h\_IRF}$ below the mean (to the right) of the best fit Gaussian to the IRF. The beginning point to which the IRF is pinned is defined as "$3x\sigma_{h\_obs}$ + 1.0m above the mean of the best fit Gaussian fit to the observed water surface returns.

4.5.5.5 Deconvolution

The "deconvolution "is solved through constrained "convolution" of the IRF histogram with the unit (or true) water profile histogram. The solution is achieved by iterating through the four parameters of the unit water profile (mean, σ_h, β and α) until the mean, standard deviation and peak of integrated histogram best matches the observed (ATLAS) histogram, as described in sections 4.5.1 through 4.5.4.

4.5.6 Estimation of coarse bottom topography, bathymetry, other subsurface anomalies

ATL13 Version 002 provides an estimate of the along track bottom topography and water depth over the telemetry range, assuming favorable water clarity and cloudless skies. The overall

approach relies on the above ATL13 analysis of surface water height combined with ideas developed by Nagle and Wright 2016,modified for ICESat-2 data.

During long segment histogramming, the vertical profile below the surface gaussian is checked for bottom and other anomalies, between the depth range of 12 standard deviations below the observed gaussian mean and the ATLAS telemetry window (20 m). The subsurface anomalies are initially computed relative to the apparent height of the normalized mean water body transect bin values. The actual subsurface or water depth is reported after correcting for refractive index (speed of light only). The algorithm is as follows:

1. The mean and standard deviation of the vertical subsurface profile for each long segment is computed. Also computed is the mean subsurface profile across all long segments in a water body transect.
2. Three anomaly threshold profiles are created; Anomaly threshold profiles, are defined as the 2* bin count of the mean subsurface histogram plus 3, 5 and 7 times the subsurface standard deviation of the subsurface bin counts of each long segment profile, respectively.
3. A subsurface anomaly profile is created corresponding to each threshold profile. For each profile, the corresponding height is identified for each occurrence when its bin value is greater than that of the threshold. The minimum height of all occurrences is then identified for each sigma level..
4. Three flags are designated “Flag 1 = Bottom or other subsurface anomaly detected”; Flag 2 = Subsurface anomaly detected, bottom possible”; Flag 3 = “Subsurface anomaly detected, bottom unlikely”
5. Whenever a long segment profile representing “2*mean+ 7*sigma” contains a minimum, it is designated as Flag 1 and its observed bin height is identified for that long segment.
6. For the remaining long-segments, when the profile representing “2*mean+5*sigma” contains a minimum, it is designated as Flag 2 and its bin height is identified for that long segment.
7. For the remaining long segments (not already determined for the 7*sigma and 5*sigma levels) above, when the profile representing “2*mean+3*sigma” contains a minimum, it is designated as Flag 3 and its bin height is identified for that long segment.
8. When no anomaly is found, designate as “No subsurface anomaly detected” or invalid.
9. The subsurface profile depths are computed as mean surface height minus the subsurface anomaly height, corrected by speed of light (multiplied by 1/1.3).

10. The bottom anomalies for ATL13 are reported for each long segment at the short segment rate. Values reported are i) the actual water depth (m) from the mean water surface, and ii) flag value.

An example of a retrieved bottom topography is shown for an ICESat-2 transect over Eagle Lake, CA on October 19, 2018. Results are reported at the subsurface rate. Additional subsurface anomalies not associated with bottom may also be detected.

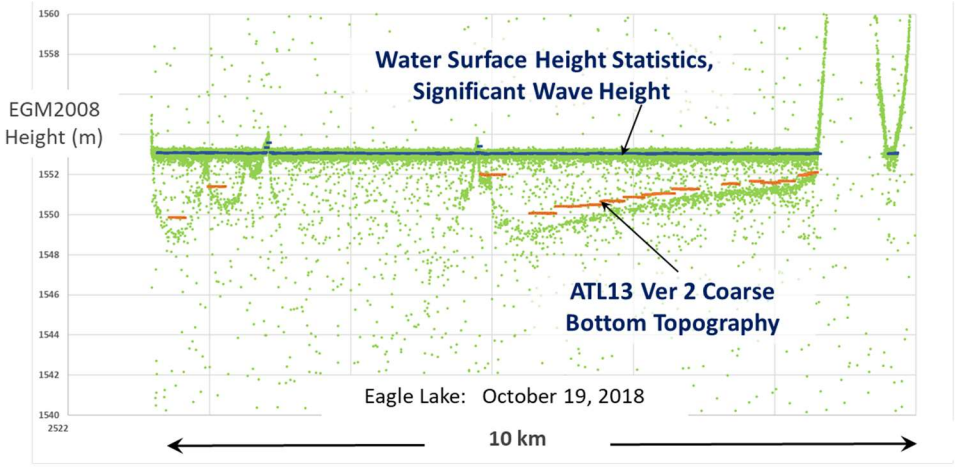

Figure 4-8 ATL13 Ver 002 identification of coarse bottom topography subsurface anomaly product.

4.6 Estimation of Mean Square Slope

Kay et al (2009) validated modeled surface by comparing their mean slopes and height standard deviation against empirical values. For mean square slope, a sample of 108 surfaces were within the range specified by Cox and Munk, or

$$\sigma_c^2 + \sigma_u^2 = \sigma_s^2 = 0.003 + 0.00512U \quad (4.13)$$

Where U is in m/s and σ_c and σ_u are in radians (dimensionless).

Kay et al compared height standard deviation to the empirical formula given by Apel (1994), confirming,

$$\sigma_h = 0.005U_{10}^2 \quad (4.14)$$

Where U10 is the 10m wind speed. Inverting 4.14 provides an estimate of the wind speed when σ_h is the unit surface profile obtained from the deconvolution algorithm. Combining 4.2, 4.13 and 4.14 yields the σ_s vs. σ_h relationship for wind driven waves,

$$\sigma_s^2 = 0.0549\sigma_h^{0.25} \qquad \sigma_h \leq 0.245 \text{ m} \quad (4.15a)$$

$$\sigma_s^2 = 0.003 + 0.0724(\sigma_h)^{0.5} \qquad 0.245 < \sigma_h \leq 0.885 \text{ m} \quad (4.15b)$$

$$\sigma_s^2 = 0.069\text{LOG}_{10}[\sigma_h] + 0.0748 \qquad 0.885 \text{ m} < \sigma_h \quad (4.15c)$$

previously plotted in Figure 4-3.

4.7 Data Product Output

The overall procedure is to process global inland water body height products and associated products based on the ATL03 processing interval. The algorithm loops through the global inland water body database organized within regional basins during each processing period, completely analyzing all the ground tracks of one water body before proceeding to the next. Along- and cross- track data products are computed for all the new ground tracks observed for that water body since the previous processing period. Inland water bodies are delineated by shape files defined in the ATL13 Inland Water Body Shape mask.

4.7.1 Single Beam Analysis

4.7.1.1 Overall Scheme:

The principal data product for each water body type consists of along track mean height, rms height, slope, 532nm attenuation coefficient and bottom anomaly depth (if observed) for short segment lengths of each strong and weak beam, although several additional products are under evaluation. The reported short segment resolution is 100 along track signal photons. Due to water and meteorology conditions, the segment length varies from approximately 30 to 100 meters. Data products are reported throughout the span of the identified water body as shown in Figure 3.3. Lidar data products are analyzed in orthometric units. Thus, data obtained from ATL03 in WGS84 ellipsoid reference data are converted to the EGM2008 Geoid.

Water bodies often have irregular shapes including dendritic or branching patterns. When an ATLAS transect crosses over a branch (completely entering then exiting the water body), then enters another branch of the same water body (completely entering and exiting), the ATL13 analyses treats and reports each crossing as separate (not connected to the first crossing), even though the water body ID is the same.

Analyses occurs as follows. The heights of long segment lengths equaling 10 sequential short segments (~1000 signal photons) are computed including deconvolution of the satellite IRF and observed water body histogram. The mean height of each short segment is adjusted based on the mean deconvolved height of the Gaussian portion of the long segment. Very long segments composed of 30 subsequent short segments (~3000 signal photons) are required for estimation of the subsurface attenuation. All short and long segments within a given very long segment are assigned the same attenuation coefficient.

4.7.1.2 Water Body Reference Identification Scheme:

Each water body is assigned a unique 10 digit descriptive reference number for each shape in the ATL13 Inland Water Body Mask. The digits are defined as follows: 1 = water body type; 2 = size range in km2; 3 = citation of water body information; 4 through 10 = unique shape ID associated with a given type. ATL13 water body types are defined as: Type 1 = lake; Type 2 = known reservoir; Type 3 = Reserved for future use; Type 4 = Ephemeral water; Type 5 = river; Type 6 = transitional water (estuary or bay); Type 7 = transitional water (coastal); Type 8 = Reserved, Type 9 = Reserved. Each type possesses unique features including shapes, sizes, depths, and water surface dynamics.

The lake size range delimitation is as follows:

Size 1: Area >10,000 km^2; Size 2: 10,000 >Area ≥1,000; Size 3: 1,000 > Area ≥100, Size 4: 100 > Area ≥10; Size 5: 10 >Area ≥1; Size 6: 1 > Area ≥0.1; Size 7: 0.01 > Area; Size 8: Reserved; Size 9: Not assigned.

The lake type and size numbers are also used internally to control processing of selected water body types and sizes.

The current citations for the Inland Water Body shapes are:

Source 1= HydroLAKES (Messager, M.L., Lehner, B., Grill, G., Nedeva, I., Schmitt, O. (2016): Estimating the volume and age of water stored in global lakes using a geo-statistical approach. Nature Communications: 13603. doi: 10.1038/ncomms13603. Data is available at www.hydrosheds.org.)

Sources 2= Global Lakes and Wetlands Database (Lehner, B. and Döll, P. (2004): Development and validation of a global database of lakes, reservoirs and wetlands. Journal of Hydrology 296/1-4: 1-22.)

Source 3= Named Marine Water Bodies (ESRI http://mappingcenter.esri.com/index.cfm?fa=arcgisResources.gisData)

Source 4=GSHHG Shoreline (Wessel, P., and W. H. F. Smith, A Global Self-consistent, Hierarchical, High-resolution Shoreline Database, *J. Geophys. Res., 101*, 8741-8743, 1996)

Sources 5 through 9 = Reserved.

Source 5= Global River Widths from Landsat (Allen and Pavelsky (2018) Global Extent of Rivers and Streams. *Science*. https://doi.org/10.1126/science.aat0636),

Sources 6=Reserved, 7=Reserved, 8=Reserved, 9=Reserved.

4.7.1.3 Contingency Analyses Due to Water Body Type and Transect Length:

Contingencies are implemented based on transect length to provide reasonable estimates of height, the main data product over the full range of water body types.

Large transects: Large transects are defined as water body crossings or portions of water body crossings equal or greater than 30 short segments (~3000 signal photons). Large transects are analyzed according to the full algorithm described in Section 4.5 and shown in Figure 5.2. Subsurface parameters are estimated using the very long segment length equal to 30 short segments. Long segments, each comprised of 10 short segments, are analyzed with the full deconvolution algorithm, while using the subsurface parameters estimated from the very long segments.

Medium transects: Medium transects are those possessing from 10 to 29 short segments. Each long segment is analyzed as in Section 4.5 and Fig. 5.2 except fixed attenuation coefficients are assumed. In the case where a previous very long segment from that water body has been analyzed, the procedure is to apply the same (subsurface) coefficients for the subsequent ~~very~~ long segment(s). If no previous very long segments have been analyzed, use default values

(α=0.5; beta=0.02). Proceed with deconvolution for long segments. For remaining 6 to 9 segments, use short segment transect contingency described below.

Short transects: Short transects are those possessing from 6 to 9 short segments. Use fixed subsurface parameters as follows. When this situation occurs after a long segment, assume the same subsurface parameters as that long segment and biases as described in 4.7.3.5. For small water bodies with no long previous long segments, report no attenuation coefficients (α, beta= invalid). Do not implement full deconvolution scheme. Rather, compute height adjustment as the difference between the mean of the Gaussian fitted to the top 80% of the observation histogram, and the mean of the Gaussian fitted to the top 50% of the IRF histogram. This difference is effectively implemented by assuming:

$$Hd = Hdss = 0. \tag{4.17a}$$

Compute the unit model σ_h as:

$$\sigma_h = \sqrt{\sigma^2_{h\_OBS\_80} - \sigma^2_{h\_IRF\_50}} \tag{4.17b}$$

Where $\sigma_h{}^2{}_{\_OBS\_80}$ is the variance of the Gaussian fitted (top 80%) to the observations and $\sigma_h{}^2{}_{\_IRF\_50}$ is variance of the gaussian fitted (top 50%) to the IRF.

If $ABS[\sigma_{h\_OBS\_80}{}^2 - \sigma_{h\_IRF\_50}{}^2] \leq 0.000025$, assume $\sigma_h = 0.005$.

If $[\sigma_{h\_OBS\_80}{}^2 - \sigma_{h\_IRF\_50}{}^2] < -0.000025$, assume σ_h = invalid.

Very Short transects (Experimental Data Product): Very short transects are those possessing from 1 to 5 short segments. When this situation occurs after a long segment, assume the same subsurface parameters as that long segment, and biases as described in 4.7.3.5. Report no subsurface parameters (α, beta= invalid) if no previous long segments. Compute height adjustment as the difference between the mean elevation of the observation photons for the

detrended segments, and the mean of the Gaussian fitted to the IRF (top 50%). This difference is effectively implemented as follows:

$$Hd = Hdss = 0. \quad (4.17c)$$

Assume H_F, H_{EM}= invalid.

For all transects (large, medium, short and very short), assign Inland Water Segment Processing Flags as described in Section 4.8.1.

4.7.1.4 Rivers

ATL13 data products over rivers are treated as a unique inland water body type (Type=5). Rivers were not provided in earlier releases due to a lack of a river shapefile mask. However, a global river mask was developed for Release 3 based on recent analyses by Allen and Pavelsky, 2018. The new ATL13 river mask will be merged with the current ATL13 Inland Water Body Mask. Typical specific features that are being be addressed are i) very long rivers that can extend over hundreds of long segments, while possessing narrow widths of only several segments, ii) meandering and braided reaches that introduce a large fraction of surface height anomalies to the transect, and iii) steep water gradients depending on terrain and the orientation of ATLAS tracks.

The overall ATL13 surface elevation retrieval scheme is the same as for other water body types. River height analyses follows that described in Section 4.7.1.2.

4.7.2 Significant Wave Height

The significant wave height, H_S, is estimated as

$$H_S = 4 * \sigma_h \quad (4.17d)$$

Where σ_h is the estimated standard deviation of the unit water surface. H_S is invalid if σ_h is invalid.

4.7.3 Estimation of Inland Water Body Bias

The solution to the deconvolution yields the modeled vertical height distribution of both the true unit water surface and the subsurface backscatter based on the processed ATLAS photon returns. The vertical height difference between the observed profile (ATLAS histogram) and the true profile (unit water surface), or bias, can arise due observation, instrument, and retrieval algorithms errors. ATL13 considers two bias errors as described below.

4.7.3.1 Goodness of Fit Bias

Bias is introduced from imperfect fit of the assumed water surface profile distribution to the observed histogram. This bias, H_F, is estimated as the difference between the centroid elevations (or equivalently the mean heights) of the observed surface water histogram, H_{OH}, and fitted integrated water surface model histogram, H_{IM} over the Gaussian range (+/- $3\sigma_h$)., or

$$H_F = H_{OH} - H_{IM} \tag{4.18a}$$

First compute the Gaussian mean and standard deviation of both the observed histogram and the integrated model histogram using its upper 80%. Then calculate the difference in centroids between the two histograms by summing over all the vertical bins within +/- 3 standard deviations of the integrated Gaussian mean, or

$$H_F = \left[\frac{\sum_{i=1}^{n} (H_{OH_i} * d_i)}{\sum_{i=1}^{n} H_{OH_i}}\right] - \left[\frac{\sum_{i=1}^{n} (H_{IH_i} * d_i)}{\sum_{i=1}^{n} H_{IM_i}}\right] \tag{4.18b}$$

where i is bin number, *n* is the total number of bins within +/- 3 standard deviations of the integrated model mean, and d_i is bin depth.

4.7.3.2 Electromagnetic Bias

Elevation error is also introduced through observation bias of the wavy surface, slope, and view angle of the detector. This observation bias, H_{EM}, is computed based on the shift in centroid of

the cross section of the joint probability density function of slope and height. Dudis (1986) derived a theoretical expression based on Longuet-Higgins (1963), or

$$H_{EM} = 3\pi S_s(\nu^2 - 1)*\sigma_h \quad (4.19)$$

where, S_s is the significant slope defined after Huang et al. (1983),

$$S_s = \sigma_h / \lambda_{pk} \quad (4.20)$$

σ_h is the standard deviation of the derived unit gaussian, and λ_{pk} is the wavelength at its spectral peak (defined in Section 4.7.3.3 below). The parameter ν is the normalized satellite view angle or

$$\nu = \theta/(\sigma_s^2)^{0.5} \quad (4.21)$$

where θ is the satellite view angle (E.g. from ATL03, nominally 0.006 rad reference track side beam need other off pointing angles) and σ_s is the root-mean-square wave slope derived in Eqn 4.15.

For the above, if σ_h is invalid, then H_{EM}, S_s, and ν are also invalid.

4.7.3.3 Wavelength and Wave Period at Spectral Peak

The wavelength at the spectral peak, λ_{pk}, is estimated from the detrended, long segment, signal photons assuming deep water. First, the parameter T_{pk_ATLAS} is estimated as the longest time between two sequential zero up-crossing wave surface signal photons within a long segment (See Figure 4-8 below for definition of zero up-crossing). Only those photons within +/- 3 σ of the detrended zero mean surface are employed. From this, the wavelength at spectral peak, λ_{pk}, and wave period at spectral peak (assumes deep water waves), T_{pk}, are estimated as

$$\lambda_{pk} = T_{pk\_ATLAS} * V_{gt} \quad (4.22a)$$

$$T_{pk} = ((\lambda_{pk}*2\pi/g)^{0.5} \quad (4.22b)$$

respectively, where g is acceleration due to gravity (9.807 m/s^2) and V_{gt} is the ATLAS ground track speed (Obtained directly from ATL03 or nominally 7000m/s).

4.7.3.4 Reported ATL13 Height Data Product

ATL13 reports heights at the short segment level. The short segment height product is computed as the sum of the following elements:

1. H_d -The adjusted height due to deconvolution of the long segments.. , i.e., the difference in mean heights between the Gaussian portions of unit water surface histogram and the integrated water surface. The mean height of the unit Gaussian water surface was previously calculated during deconvolution. The mean height of the integrated water surface is computed as the mean of only the Gaussian portion of the observed, detrended and binned, signal photons, calculated over the top 80% (or 2.5*Sigma). This is set $H_d = 0$.

For short transects, assume Hd = Hdss = as defined in Section 4.7.1.2, Equations 4.17a and 4.17c.

2. The H_F and H_{EM} biases.

3. H_M - The mean of the surface signal photons originally defined by the mode of the short segment heights before detrending. Only the surface signal photons of each segment that fall within +/- 3 sigma of the short segment mode (using the integrated histogram sigma) are used in the calculation of the mean.

The ATL13 reporting elevation in orthometric units (EGM2008) is,

$$H_{ATL13\_EGM2008} = H_M + H_d + H_F - H_{EM}. \quad (4.23a)$$

If H_F is designated invalid, then replace Eqn. 4.23a with 4.23b below,

$$H_{ATL13\_EGM2008} = H_M + H_d + H_{EM.} \quad (4.23b)$$

If H_F and H_{EM} are both designated invalid, then replace Eqn. 4.23a with 4.23c below,

$$H_{ATL13\_EGM2008} = H_M + H_d. \quad (4.23c)$$

The ATL13 reporting elevation above the ellipsoidal height (WGS84) is also provided, or

$$H_{ATL13\_WGS84} = H_{ATL13\_EGM2008} + H_{GeoidEGM2008}. \quad (4.24)$$

In any case where either $\mathbf{H_F}$, $\mathbf{H_{EM}}$, or both are invalid, they are excluded from the calculation of short segment height.

The height and geolocation are reported at the closest signal photon location.

4.7.3.5 Contingency for transects less than one long segment.

If the number of short segments is less than the ten required for one long segment but is preceded by a complete long segment, then assume that within Eqn 4.23a, H_F and H_{EM} are equal to that in the previous long segment. If the number of short segments is less than the ten required for one long segment and is not preceded by a complete long segment, then assume that H_F and H_{EM} are invalid.

4.7.3.6 First photon bias correction.

First photon bias (FPB) is the term applied to the reduction in the number of received photons actually recorded by the ATLAS detectors for high photon rates of return. This can occur for each detector for a short interval of time after a series of initial photon are received. The actual count is thus biased on the low side and depends on the rate of return.

ATL13 provides a correction for users to apply, as it is not automatically applied. It corrects the estimated mean water surface height in Equations 4.23 and 4.24 using the FPB correction procedure outlined in the CAL_19 Calibration Product of ATL03. The following steps are employed: First, the apparent width of the full-width half-max (FWHX) standard deviation of the ATL13 surface is computed based on the previously estimated standard deviation (σ_h) or

$$\sigma_{h\_OBS\ FWHM} = 2.355\ \sigma_{h\_OBS\_80} \quad [m] \qquad 4.24b$$

or in terms of time of flight $\sigma_{h\_OBS\ FWHM} = 15.7*\sigma_{h\_OBS\_80}$ [ns] 4.24c

(where, in Chapter 5, $\sigma_{h\_OBS\_80}$ = *detrend_sigma2* for long segments or *L_surf_inc_stdev2* for contingency cases), and converted time of flight by 2*3.333 ns/m. Second, the apparent strength of the return in terms of photons/shot is estimated based on the previously computed short segment photon rate, or

Strength_ATL13 sseg = s_seg1*0.7/Length_sseg [pe/shot] 4.24d

where 0.7 equals spacecraft velocity (m/s) divided by 10,000 or distance per Atlas shot. Third, dead time is assumed equal to the mean of the detectors used for each beam. Fourth, the FPB correction, or ffb_corr from ATL03, is obtained in terms of native ps units. Finally, the mean short segment water surface height FTB correction is estimated in cm as

Segment_fpb_correction = 0.00015 * ffb_corr [m] 4.24e

Note: The user should subtract the_fpb_correction from the mean height products such as ht_ortho (EGM2008) and ht_water_surf (WGS84). The above correction is not applied when all detectors are saturated. A correction for such severely biased returns is anticipated in ATL13 Release 4.

4.7.4 **Dynamic Atmospheric Correction and Ocean Tides**

Three fields associated with dynamic atmospheric correction and ocean tides were added to the output table. They include: i) the Dynamic Atmospheric Correction (DAC) that includes inverted barometer (IB) effect (±5 cm), ii) the ocean tides that include diurnal and semi-diurnal (harmonic analysis (±4 m), and iii) the long period equilibrium tide self-consistent with ocean tide model (± 0.04 m). Although the above values are made available at short segment rate for all water body types, they are not included in the standard inland water height products, They are provided

mainly for convenience use at user's discretion, for possible use with the transitional tidal and coastal water (types 6 and 7) and the largest lakes of Type 1 (~> 10,000 km^2).

4.8 Quality and classification flags throughout flow of analysis

Quality flags are provided at the following steps in the analysis:

4.8.1 Inland Water Segment Processing Flag

This flag describes the level of processing using to estimate the surface and subsurface parameters. Set Flags as follows:
= 7 designates 30 or more short segments analyzed using the full deconvolution scheme,
= 6 designates10 to 29 short segments used,
= 5 designates 8 to 9 short segments used,
= 4 designates 6 to 7 short segments used
= 3 designates 3 to 5 short segments used
= 2 designates 2 short segments used
= 1 designates 1 short segment used.

4.8.2 Background Flag

This flag describes the intensity of the background rate in each short segment. The flags are:

= 0 if ***bckgrd_dnsty_50sht_bin_Sseg*** $\leq$ ***bckgrd_dnsty_threshold1***

= 1 if ***bckgrd_dnsty_threshold1*** > ***bckgrd_dnsty_50sht_bin Sseg*** $\leq$ ***bckgrd_flag_threshold2***

= 2 if ***bckgrd_dnsty_threshold2*** > ***bckgrd_dnsty_50sht_bin Sseg*** $\leq$ ***bckgrd_dnsty_threshold3***

= 3 if ***bckgrd_dnsty_threshold3*** > ***bckgrd_dnsty_50sht_bin Sseg*** $\leq$ ***bckgrd_dnsty_threshold4***

= 4 if ***bckgrd_dnsty_threshold4*** > ***bckgrd_dnsty_50sht_bin Sseg*** $\leq$ ***bckgrd_dnsty_threshold5***

= 5 if ***bckgrd_dnsty_threshold5*** > ***bckgrd_dnsty_50sht_bin Sseg*** $\leq$ ***bckgrd_dnsty_threshold6***

= 6 if ***bckgrd_dnsty_50sht_bin*** > ***bckgrd_dnsty_threshold6***

bckgrd_dnsty_threshold1 = 0.001 (counts per bi per Lseg)
bckgrd_dnsty_threshold2 = 0.010 (counts per bin per Lseg)
bckgrd_dnsty_threshold3 = 0.050 (counts per bin per Lseg)
bckgrd_dnsty_threshold4 = 0.10 (counts per bin per Lseg)
bckgrd_dnsty_threshold5 = 0.300 (counts per bin per Lseg)
bckgrd_dnsty_threshold6 = 0.500 (counts per bin per Lseg)

4.8.3 **Bias Fit Flag**

The bias fit flag

= -3 when $H_F < -0.10$ (m)
= -2 when $-0.10 \leq H_F < -0.05$
= -1 when $-0.05 \leq H_F < -0.01$
= 0 when $-0.01 \leq H_F < 0.01$ (m)
=1 when $0.01 \leq H_F < 0.05$
=2 when $0.05 \leq H_F < 0.10$
=3 when $0.10 \leq H_F$
=4 when H_F is invalid.

4.8.4 **EM Bias Flag**

The EM Bias Flag is defined as follows:

= -3 when $H_{EM} < -0.10$ (m)
= -2 when $-0.10 \leq H_{EM} < -0.05$
= -1 when $-0.05 \leq H_{EM} < -0.01$
= 0 when $-0.01 \leq H_{EM} < 0.01$ (m)
=1 when $0.01 \leq H_{EM} < 0.05$
=2 when $0.05 \leq H_{EM} < 0.10$
=3 when $0.10 \leq H_{EM}$
=4 when H_{EM} is invalid.

4.8.5 **Short Segment Length Flag**

The Short Segment Length Flag is defined as follows:
= 0 when SSL < 50 m
= 1 when 50 ≤ SSL < 150 m
= 2 when 150 ≤ SSL < 300 m
= 3 when SSL ≥ 300 m

4.8.6 **Long Segment Length Flag**

= 0 if ***Lseg_length*** < 500 (meters)

= 1 if 500 ≤ ***Lseg_length*** < 1500 (meters)

= 2 if 1500 ≤ ***Lseg_length*** < 3000 (meters)

= 3 if 3000 ≤ ***Lseg_length***

4.8.7 **Clouds Flag**

Cloud confidence flags derived in ATL09 are convert to ATL13 short segment rates using a nearest neighbor approach. They include Cloud_Flag_ASR, Cloud_Flag_Atm and Layer_Flag.

4.8.8 **Flags Associated with Snow and Ice**

The ATL13 snow and ice flags are (snow_ice_ATL09), obtained from the ATL09 Snow_Ice flag and the NOAA GMASI product, are assigned at the short segment rate as: 0 = ice free water, 1 = snow free land, 2 = snow, and 3 = ice. When there is more than one overlap, they are assigned the greatest value.

4.8.9 **Flags Associated with Surface Temperature**

ATL13 reports the ATL09 MET surface (skin) temperature at the short segment rate based on a linear interpolated nearest neighbor approach.

4.9 Data Product Precision and Evaluation

The Inland Water Data Product quality relies on the precision of the ATL03 georeferenced photons and associated products which are evaluated prior to their use within ATL13. The plan for evaluating ATL13 data products is presented in Section 4.9.2.

4.9.1 ICESat-2 Precision

The precision of the ICESat-2 retrieval is estimated from root mean square of five error sources:

i) Radial orbit error, RO_{RMS}
ii) Tropospheric delay error, TD_{RMS}
iii) Forward scattering error, FS_{RMS}
iv) Geolocation Knowledge uncertainty, GK_{RMS}
v) ATLAS ranging precision per photon, σ_{RMS}.

Actual rms error for each source are obtained from ATL03. The current default values are RO_{RMS} = 4.0 cm, TD_{RMS} = 3 cm, FS_{RMS} = 3 cm, GK_{RMS} <0.5 cm (over water) and σ_{RMS} = 24.0 cm. For 100 photon short segments, the ranging precision is estimated as $\sigma_{RMS100} = \sigma_{RMS}/(100^{1/2}) = 24/(100)^{1/2}$ = 2.4 cm.

The overall ensemble error per 100 inland water photons is estimated as

$$\sigma_{ICESat2} = \sqrt{[RO_{RMS}^2 + TD_{RMS}^2 + FS_{RMS}^2 + GK_{RMS}^2 + \sigma_{100\ shots}^2]}$$
$$= \sqrt{37.25} = 6.1 \text{ cm} \quad (4.29)$$

This precision error is updated as post-launch ATLAS data sets are evaluated.

Previously analyzed MABEL data (Jasinski et al., 2016) scale well with the anticipated ATLAS observations. Results indicate a MABEL water return rate of 0.36 to 2.90 pe/m depending on surface and atmospheric conditions. The ranging precision for a 100 shot segment would vary from 2.0 to 5.0 cm, respectively.

4.9.2 Data Product Evaluation

A plan for evaluating the Inland Water Data Product has been formulated during the development of ATL13 by collaborating with relevant U.S. agencies, university researchers, and other various organizations. Data product quality is achieved through monitoring, assessment

and validation at various levels of effort depending on available resources. The overall approach is i) to compare ATL13 data products with *in situ* data and satellite radar altimetry where available, ii) evaluate several components of the ATL13 algorithm through threshold monitoring with model diagnostics, and iii) conduct in situ validation and calibration when resources are available or synergistic field opportunities arise. Evaluation will be conducted over all ATL13 Inland Water Body types including lakes, reservoirs, rivers, estuaries and near shore coasts. Sites are located primarily in the US and North America, but also at several international sites. Every effort is made to be aware of, and participate in, other sponsored field programs by NASA and other agencies including satellite mission CAL/VAL plan.

4.9.2.1 Monitoring Activities

Monitoring refers to active and continuous evaluation of ICESat-2 data-product parameters, primarily through data visualizations and threshold monitoring. Monitoring will occur through comparison of ATL13 time series data plots with other independent data. Time series will be evaluated with respect to mean water surface segment heights, variances, slopes, significant wave height, subsurface attenuation, presence of ice, and identifiable bottom location, as a function of water body type, location, water clarity and prevailing meteorological conditions. For the Inland Water Data Product, monitoring occurs principally by leveraging off existing databases supported by numerous organizations in the US and internationally, including radar altimetry missions. Principal sources include:

a) Reservoir and lake elevations based on satellite radar altimetry from Jason 3, Sentinel 3A and 3B sensors and compiled at online archives. Example online data bases include:

i) HYDROWEB (Theia, LEGOS, other international)

http://hydroweb.theia-land.fr

ii) Center for Topographic Studies of the Ocean and Hydrosphere (CTOH)

http://ctoh.legos.obs-mip.fr/products/hydroweb

iii) Global Reservoir and Dam Database (GWSP)

http://www.gwsp.org/products/grand-database.html

iv) G-REALM (USDA)

https://ipad.fas.usda.gov/cropexplorer/global_reservoir

v) Global River Database

http://gaia.geosci.unc.edu/rivers/

vi) River and Lakes (ESA) (historical data)

http://tethys.eaprs.cse.dmu.ac.uk/RiverLake/shared/main

b) *In situ* water level gauges primarily at reservoirs, lakes, and other water bodies monitored by the: i) US Geological Survey (USGS), ii) National Oceanic and Atmospheric Administration (NOAA), iii) Bureau of Land Management (BLM), and iv) US Army Corps of Engineers (USACE). Although there are hundreds of available sites, the principal water bodies being considered include Lake Fort Peck, MT; Lake Mead, NV; all Great Lakes; Lake Tahoe, CA; Chesapeake Bay; Lake Teshekpuk and Toolik Lake, AK; Lake Issyk-Kul, Kyrgyzstan; water bodies within the Mississippi, Connecticut, and Yukon River basins. All these water bodies are well gaged by the USGS, NSF, or other US agencies with accessible online data. Analyses will include evaluation mainly of root mean square error, bias, and mean absolute error. Databases include:

i) NOAA Great Lakes Environmental Research laboratory

https://www.glerl.noaa.gov/data/wlevels/levels.html#observations

i) Lake Levels (GWSP)

http://www.lakelevels.info

ii) Lakes Online

http://www.lakesonline.com/

iii) USGS National Water Information System

https://waterdata.usgs.gov/nwis

4.9.2.2 Assessment and Validation Activities

Assessment refers to a single post-launch evaluation of ICESat-2 data-product accuracy and/or precision, generally against in situ data. Validation' refers to an aggregate of post-launch 'assessments' to determine global ICESat-2 accuracy or precision. Instruments will be included that observe water surface height statistics, wind speed and direction, and basic water quality

constituents that affect optical transmission and turbidity such as mineral particles, dissolved organic carbon and chlorophyll, among others.

Several opportunities have been planned with the following programs:

a) United States Great Lakes and near shore transitional zones. Field experiments are planned in collaboration with the Joint Airborne Lidar Bathymetry Technical Center of Expertise (JALBTCX) mission performs operations, research, and development in airborne lidar bathymetry to support the coastal mapping and charting requirements of the US Army Corps of Engineers (USACE), the US Naval Meteorology and Oceanography Command, the National Oceanic and Atmospheric Administration (NOAA), and the U.S. Geologic Survey (USGS). JALBTCX executes survey operations worldwide using the Coastal Zone Mapping and Imaging Lidar (CZMIL) system and other industry-based coastal mapping and charting systems. CZMIL is integrated with an ITRES CASI-1500 hyperspectral imager and a true-color digital camera. CZMIL collects 10-kHz lidar data concurrent with 5-cm digital true-color and 48-band hyperspectral imagery. JALBTCX research and development supports and leverages work in government, industry, and academics to advance airborne lidar and coastal mapping and charting technology and applications. An example of planned JALBTCX coverage in 2018 and 2019 is shown below.

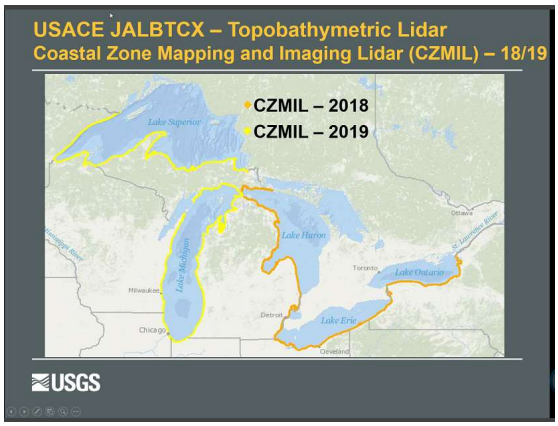

b) Alaska Sites

ATL13 has planned collaboration with researchers from the Alaska USGS, the University of Alaska, Fairbanks, and NASA GSFC, for in situ monitoring during overflights. Sites include NSF sponsored Lakes Teshekpuk and Inigot, Toolik Lake; and the Yukon River and the

Mackenzie River deltas as shown below. Participation in NASA GSFC field experiments at the mouths of the Yukon River and the near-shore region off Northern Alaska to the Mackenzie River mouth are currently under consideration.

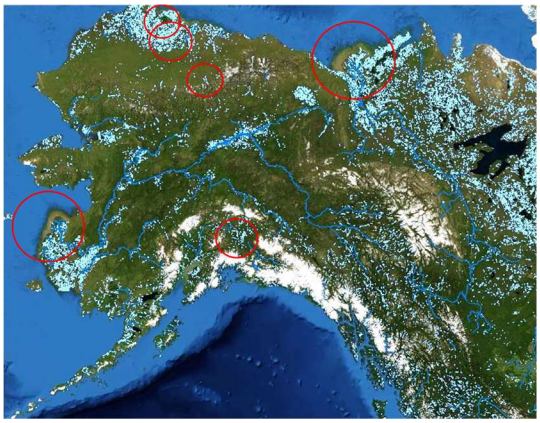

c) Mid-Latitude Lakes and Reservoirs

Assessment sites include collaboration a several sites with various groups including the Great Lakes (JALBTCX, Illinois State geological Survey), Lakes Mead (US Bureau of Reclamation), Lake Fort Peck (USACE), Lake Tahoe and Western Lake Erie (Kent State). For the Great Lakes, ATL13 is collaborating with efforts to measure Great Lakes surface water conditions at the locations shown below.

d) Transitional Water Bodies (Estuaries, Bays, Near Shore Coasts)

Principal areas would include the Chesapeake Bay, and the estuaries of the Mississippi/Atchafalaya River deltas, Everglades, Mackenzie River, and Yukon River, together with the near shore regions surrounding the East and West coast of the continental U.S. and Northern Alaska.

Collaboration with personnel from NOAA STAR for in situ measurements on the Chesapeake Bay is planned.

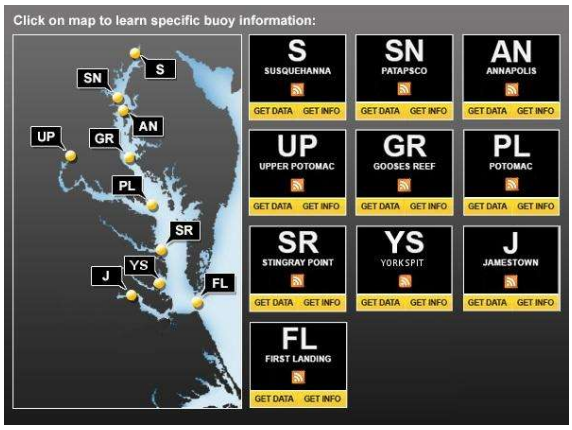

4.9.2.3 Calibration Activities and Measurements

Data product calibration consists of the application of post-launch 'assessments' or 'validations' to either ICESat-2 instrument settings, or to future data releases, in an effort to improve measurement accuracy and/or precision. Necessary measurements for validation include the following:

i) Meteorology: Wind speed and direction, optical depth, cloud cover

ii) Water Surface Physical Properties: GPS, wave height statistics, temperature, water depth

iii) Subsurface Radiative Properties: Subsurface upwelling and downwelling radiance, at 532 nm.

iv) Water Inherent Optical Properties: subsurface attenuation, suspended particulate matter, CDOM, Chlorophyll, temperature, salinity, turbidity (NTU) and Secchi Depth.

4.10 ATL22 Mean Transect Products (To be released in 2020)

All ATL13 products for each water body crossing transect up to now have been reported at the short segment level. However, in many cases, users focused on both science and applications may require products associated with the overall transect. These will include, for instance, overall crossing width, bank elevation at beginning and end of crossing, or mead water level across the transect. These products, to be reported as ATL22, are being built from ATL13 data products, taking advantage of the current Version 3 analyses ATL13 products that are anticipated to be released in ATL22 are provided in Table 5-3.

5.0 ALGORITHM IMPLEMENTATION

5.1 Outline of Procedure

The overall procedure is to process global inland water bodies on a regular basis based on the ATL03 processing interval. The algorithm loops through the global inland water body database organized within regional basins, during each processing period, completely analyzing all the ground tracks of one water body before proceeding to the next. Along- track data products are computed for all the new ground tracks observed for that water body since the previous processing period.

Inland water bodies are delineated by shape files defined in the ATL13 Inland Water Body Shape mask. Inland water bodies include lakes, reservoirs, rivers, and transitional waters including estuaries, bays, and near coasts. The Regional Basin contains all the water bodies within its boundaries.

Specific steps in the implementation of the Inland Water Body Height algorithm are detailed below. Overview and detailed flowcharts are provided in Figures 5-1 and 5-2, respectively.

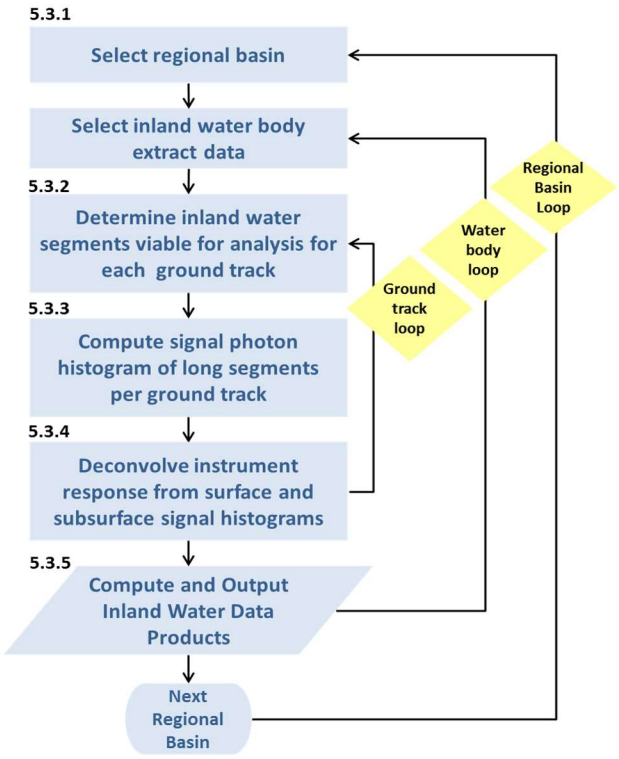

Figure 5-1 Overview Flowchart of Inland Water Height Algorithm for ATL13.

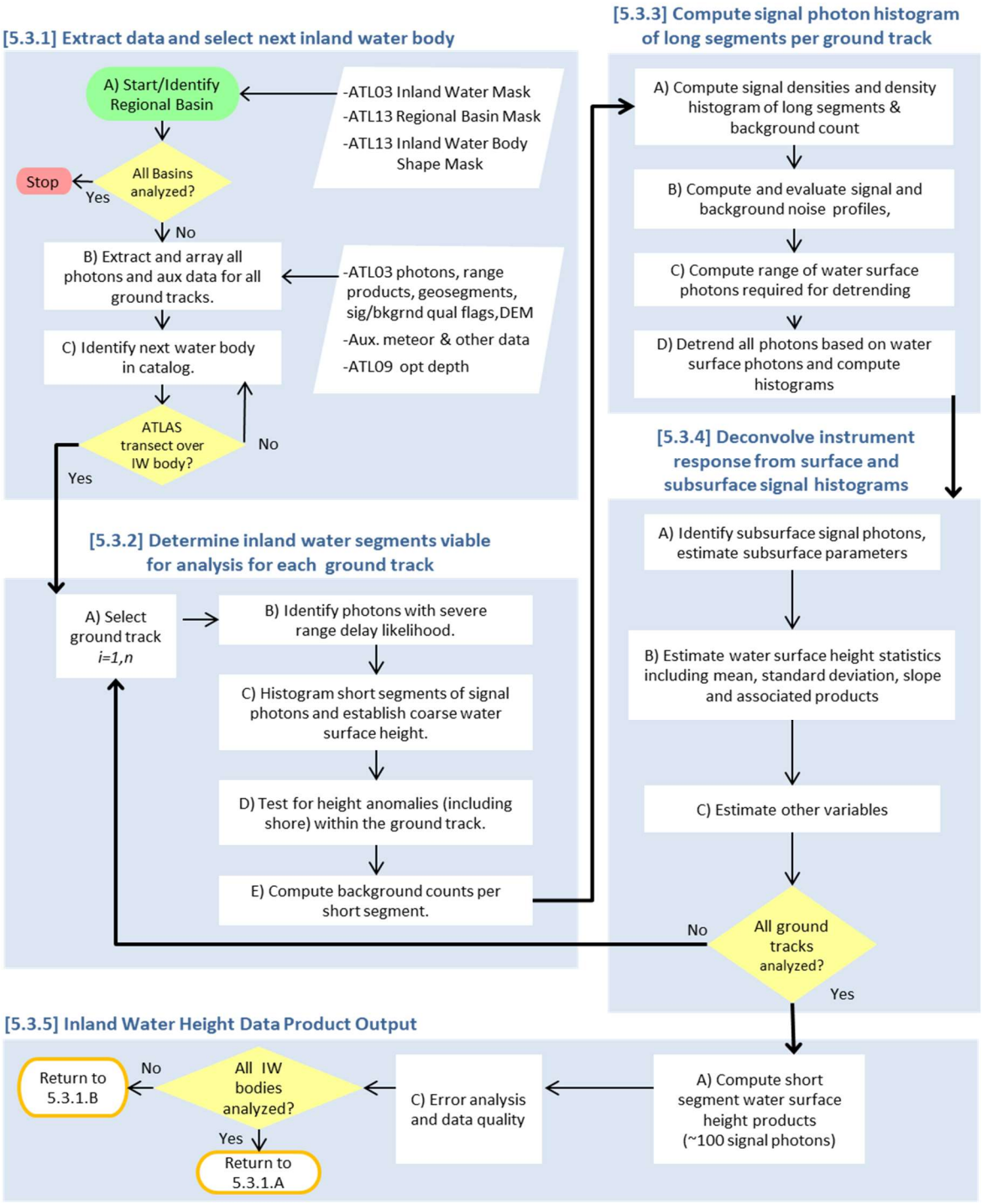

Figure 5-2 Detailed Flowchart of Inland Water Height Algorithm for ATL13.

5.2 ATL13 Inland Water Output Variables

Table 5-1 ATL13 Inland Water Along Tract Output Parameters

Name	Units	Description
ATL13_reference_id	N/A	Unique aggregate reference number for each shape in the ATL13 Inland Water Body Mask, where digit 1 = type, digit 2 = size, digit 3 = source, and digits 4-10 = shape id
inland_water_body_id	N/A	Identifying signature of an individual inland water body. Each body of water is represented by a unique numeric value.
inland_water_body_type	N/A	Type of Inland Water Body, where 1=Lake, 2=Known Reservoir, 3=(Reserved for future use), 4=Ephemeral Water, 5=River, 6=Estuary or Bay, 7=Coastal Water
inland_water_body_size	N/A	Size of Inland Water Body, where 1=Area>10,000 km^2, 2=10,000>A≥1,000, 3=1,000>A≥100, 4=100>A≥10, 5=10>A≥1, 6=1>A≥0.1, 7=0.01>A, 9 = Not Assigned
inland_water_body_source	N/A	Source of Inland Water Body shape, where: 1= HydroLAKES (Messager, M.L., Lehner, B., Grill, G., Nedeva, I., Schmitt, O. (2016): Estimating the volume and age of water stored in global lakes using a geo-statistical approach. Nature Communications: 13603. doi: 10.1038/ncomms13603. Data is available at www.hydrosheds.org.) 2= Global Lakes and Wetlands Database (Lehner, B. and Döll, P. (2004): Development and validation of a global database of lakes, reservoirs and wetlands. Journal of Hydrology 296/1-4: 1-22.) 3= Named Marine Water Bodies (ESRI http://mappingcenter.esri.com/index.cfm?fa=arcgisResources.gisData) 4=GSHHG Shoreline (Wessel, P., and W. H. F. Smith, A Global Self-consistent, Hierarchical, High-resolution Shoreline Database, *J. Geophys. Res., 101*, 8741-8743, 1996) 5=Global River Widths from Landsat (Allen and Pavelsky (2018) Global Extent of Rivers and Streams. *Science*. https://doi.org/10.1126/science.aat0636), 6=Reserved, 7=Reserved, 8=Reserved, 9=Reserved

Name	Units	Description
iw_bdy_region	N/A	ATL13-created shapefile representing relevant bodies of water over which to implement the ATL13 water surface finding algorithm only within a region of processing interest
ht_water_surf	meters	Water surface height, reported for each short segment (default length = approximately 100 signal photons) with reference to WGS84 ellipsoid
segment_lat	degrees	Latitude of reporting location for all short segment statistics
segment_lon	degrees	Longitude of reporting location for all short segment statistics.
segment_delta_time	seconds	Time of reporting for all short segment statistics.
segment_geoid	meters	Applicable geoid value at reporting location for all short segment statistics.
sseg_mean_lat	degrees	Mean latitude of the signal-qualified photons in a short segment (deferred).
sseg_mean_lon	degrees	Mean longitude of the signal-qualified photons in a short segment (deferred).
sseg_mean_time	seconds	Mean time of the signal-qualified photons in a short segment (deferred).
segment_dac	meters	Dynamic atmospheric correction (DAC) includes inverted barometer (IB) effect (±5 cm). Although available at short segment rate for all water body types, value is provided mainly for transitional tidal and coastal water (types 6 and 7) and the largest lakes of Type 1 (~> 10,000 km^2) for user's discretion.
segment_tide_ocean	meters	Ocean tides including diurnal and semi-diurnal (harmonic analysis (±4 m). Although available at short segment rate for all water body types, value is provided mainly for transitional tidal and coastal water (types 6 and 7) and the largest lakes of Type 1 (~> 10,000 km^2) for user's discretion.

Name	Units	Description
segment_tide_equillibrium	meters	Long period equilibrium tide self-consistent with ocean tide model (± 0.04 m). Although available at short segment rate for all water body types, value is provided mainly for transitional tidal and coastal water (types 6 and 7) and the largest lakes of Type 1 (~> 10,000 km^2) for user's discretion.
subsurface_attenuation	m^{-1}	Subsurface attenuation coefficient, reported per long segment (default length = 10 short segments = approximately 1000 signal photons).
segment_slope_trk_bdy	unitless	Along track water body surface slope, reported per short segment ID per water body.
ht_ortho	meters	orthometric height EGM2008 converted from ellipsoidal height.
stdev_water_surf	meters	Derived standard deviation of water surface, calculated over long segments (when available) with result reported at each short segment location tag contained within.
sig_wv_ht	meters	Significant wave height (per short segment)
water_depth	meters	Depth from the mean water surface to detected bottom.
sseg_err_ht_surf	meters	Precision per 100 inland water photons: Eqn 4.2.9
err_slope_trk	unitless	Error included in segment_slope_trk_local. (deferred)
QF_IwP	unitless	Describes the level of processing the inland water algorithm was able to perform based on the data available, ranging from zero to 3.
QF_Cloud	unitless	passedPassed through quality flag from ATL09 (zero to 5), not implemented in ATL13 Ver 1.
QF_Bckgrd	unitless	Describes the degree of background photons present in each short segment. (Update wrt/ the sseg average bckgrd_count_flag)

Name	Units	Description
Ice_Flag	unitless	Describes likelihood of ice on water surface short segment. (Not calculated in Release 3. Set = 0)
QF_Ice	unitless	Describes likelihood of ice on water surface short segment. (Not calculated in Release 3. Set = invalid)
QF_Subsurf_Anom	unitless	See Sect isubsurface anomaly on 4.8.5-9. Reported for each bin in observed histogram
QF_Bias_Fit	unitless	Goodness of fit anomaly
QF_Bias_EM	unitless	EM bias anomaly
QF_Spec_Width	unitless	Spectral width flag
QF_Sseg_Length	unitless	Length of short segments flag
QF_Lseg_Length	unitless	Length of long segments flag (reported at short segment)
met_wind10_ATL09	m/s	Wind speed magnitude at 10m height from ATL09 input.
met_wind10_ATL13	m/s	Wind speed at 10m height, based on derived water surface wave height.
met_ts_ATL09	K	Surface (skin) temperature from ATL09
snow_ice_ATL09	unitless	NOAA snow/ice flag scaled by ATL09 (0=ice-free water, 1=snow-free land, 2=snow, 3=ice)
Cloud_Flag_ASR_ATL09,	unitless	Cloud probability from ASR
Cloud_Flag_Atm_ATL09	unitless	Cloud flag from backscatter profile

Name	Units	Description
Layer_Flag_ATL09	unitless	Consolidated cloud flag
segment_fpb_correction	meters	First photon bias correction. May be applied at user disrection by subtracting from mean height produts ht_ortho and ht_water_surf.
transect_ID	unitless	Transect within a water body to which the short segment rate output belongs.
sseg_start_lat	degrees	Latitude at which the short segment begins. May be a signal or non-signal photon.
sseg_start_lon	degrees	Longitude at which the short segment begins. May be a signal or non-signal photon.
sseg_end_lat	degrees	Latitude at which the short segment ends. May be a signal or non-signal photon.
sseg_end_lon	degrees	Longitude at which the short segment ends. May be a signal or non-signal photon.
segment_full_sat_fract	unitless	The fraction of pulses within the short segment determined to be fully saturated based on ATL03 geosegment rate input.
segment_near_sat_fract	unitless	The fraction of pulses within the short segment determined to be nearly saturated based on ATL03 geosegment rate input.
segment_azimuth	radians	The direction, eastwards from north, of the laser beam vector as seen by an observer at the laser ground spot viewing toward the spacecraft (i.e., the vector from the ground to the spacecraft). When the spacecraft is precisely at the geodetic zenith, the value will be 99999 degrees.

5.3 ATL22 Output Variables (Future Transect Mean Products)

This section describes the inland water variables that will be developed as a basis for overall transect mean and related products, to be provided in 2020.

Table 5-2 ATL22 Transect Mean and Related Output Parameters (Future Product)

Name	Units	Description
ATL13_reference_id	N/A	Unique aggregate reference number for each shape in the ATL13 Inland Water Body Mask, where digit 1 = type, digit 2 = size, digit 3 = source, and digits 4-10 = shape id
transect_mean_lat	degrees	Reporting latitude of transect statistics, calculated as mean of all reported sseg latitudes in the transect.
transect_mean_lon	degrees	Reporting longitude of transect statistics, calculated as mean of all reported sseg longitude in the transect.
transect_mean_time	sec	Reporting time of transect statistics, calculated as mean of all reported sseg time in the transect.
transect_sseg_cnt	N/A	Number of non-anomalous short segments in the transect.
transect_lseg_cnt	N/A	Number of complete long segments in the transect.
transect_lseg2_cnt	N/A	Number of complete very long segments in the transect.
transect_start_lat	degrees	Latitude of the transect start, determined by the latitude of the first photon in the first short segment in the transect.
transect_start_lon	degrees	Longitude of the transect start, determined by the longitude of the first photon in the first short segment in the transect.
transect_start_time	seconds	Time of the transect start, determined by the time of the first photon in the first short segment in the transect.
transect_end_lat	degrees	Latitude of the transect end, determined by the latitude of the last photon in the last short segment in the transect.
transect_end_lon	degrees	Longitude of the transect end, determined by the longitude of the last photon in the last short segment in the transect.
transect_end_time	seconds	Time of the transect end, determined by the time of the last photon in the last short segment in the transect.
transect_mean_ht_WGS84	meters	Mean geodetic height of the transect with respect to the WGS84 ellipsoid, determined as the mean of all reported short segment height values in the transect.

Name	Units	Description
transect_mean_ht_ortho	meters	Mean orthometric height of the transect with respect to the EGM2008 geoid, determined as the mean of all reported short segment height values in the transect.
transect_mean_stdev_water_surf	meters	Mean standard deviation of the transect water surface.
transect_mean_subsurf_atten	m^{-1}	Mean subsurface attenuation (alpha) of the transect, determined as the mean of all reported alphas along the transect.
transect_length	meters	Length of the transect, determined as the distance from the first observed reference photon in the water body to the final observed photon in the body.
transect_percent_mask_width	N/A	Percent of water body mask width observed by ATLAS crossing.
transect_start_sseg_idx	N/A	Index of first entry in ATL13 short segment rate output data contributing to transect summary.
transect_end_sseg_idx	N/A	Index of final entry in ATL13 short segment rate output data contributing to transect summary.
max_slope	N/A	Maximum slope of planar triangular surface between adjacent strong beams (deferred).
aspect	rad	Direction of slope of planar surface with respect to North between adjacent strong beams (deferred)
plan_lat	degrees	Latitude of reporting location for multi-beam planar statistics (deferred)
plan_lon	degrees	Longitude of reporting location for multi-beam planar statistics (deferred)
err_slope_bdy	unitless	Error included in segment_slope_trk_bdy. (deferred)
err_aspect	rad	Error included in aspect reported. (deferred)

6.0 PRE-LAUNCH DATA PRODUCT RESULTS USING HIGH ELEVATION AIRBORNE PROTOTYPE ATLAS OBSERVATIONS

6.1 Typical ATL13 examples using MABEL

Given that MABEL's sampling design scales well with ATLAS, it has proven to be an important instrument for testing the ATL13 algorithm. This section summarizes the results of three diverse applications of ATL13 to the high elevation MABEL photon counting data (Jasinski et al., 2016). The cases include one estuary, the Chesapeake Bay; one coastal region, the Atlantic Ocean at Virginia Beach; and one reservoir, Lake Mead including bathymetry identification. Cases also differ by time of overflight and turbidity.

6.1.1 Inland Estuary – Chesapeake Bay

The Chesapeake Bay transects is shown in Figure 6.1. The case represents a mid-day observation on September 25, 2013 with moderate wind and turbidity with mostly clear sky conditions. The transect consists of a one minute acquisition along an 8 km reaches in the middle of the bay near NOAA's Gooses Reef buoy. There were no land crossings and water depth was greater than 10 m.

Plots of the georeferenced MABEL photon cloud returns from the atmosphere through the water column with respect to the WGS84 Geodetic height are shown in Figure 6.2.

.

Figure 6-1 Location map of high altitude MABEL flights over Chesapeake Bay in 2013 near Gooses Reef buoy. Base map from Google Earth

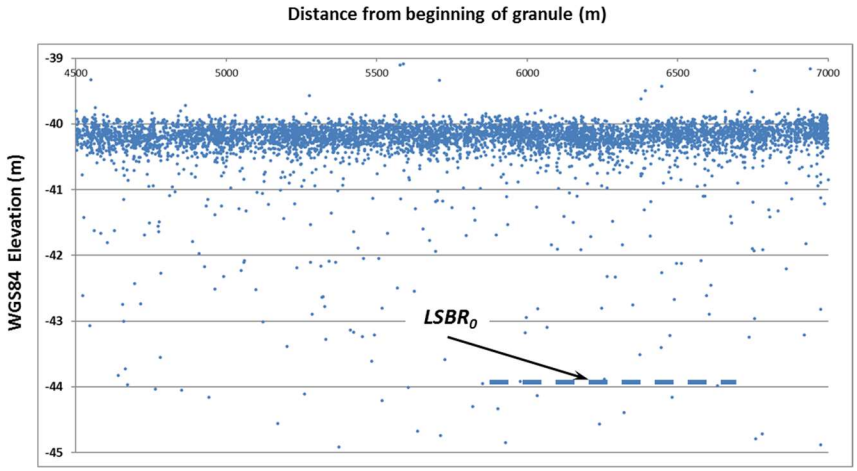

Figure 6-2 MABEL 2013 data, Chesapeake Bay Near Gooses Reef buoy. (Jasinski et al., 2016)

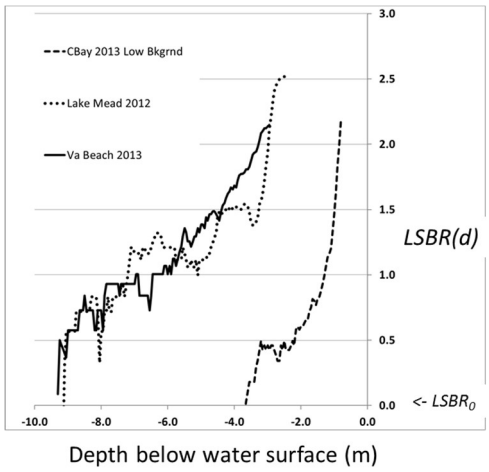

Figure 6-3 Signal to background ratio profiles versus depth, LSBR(d), for cases presented in this study, expressed in Log_{10} base. Also indicated is the $LSBR_0$ threshold level. (Jasinski et al., 2016).

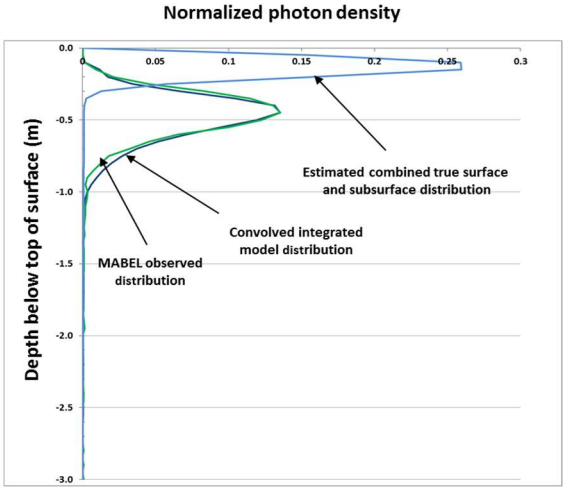

Figure 6-4 Histograms of the components of the best fit convolution model for Chesapeake Bay case (Jasinski et al., 2016)

6.1.2 Near Shore – Atlantic Ocean at Virginia Beach

This case is an East-West transect extending from the Atlantic coast at Virginia Beach, just south of the mouth of the Chesapeake, eastward into the Atlantic on September 19, 2013 at 22:30 UTC (late afternoon local time). Figure 6.5 shows the transect location map which is situated just south of the mouth of the Chesapeake Bay. A 20 second segment of about 2000 MABEL photons is plotted in Figure 6.6. For this date, sky conditions were mostly clear, and wind from the East at 4.2 m/s. One additional feature not seen in the Chesapeake Bay cases is evidence of some wave structure throughout the transect. This is attributed to the MABEL flight being aligned nearly parallel to the wind direction. Histograms of the MABEL and integrated model are shown in Figure 6.7

Figure 6-5 Location map of high altitude MABEL flights over Site 2, Atlantic Ocean near Virginia Beach. Base map from Google Earth.

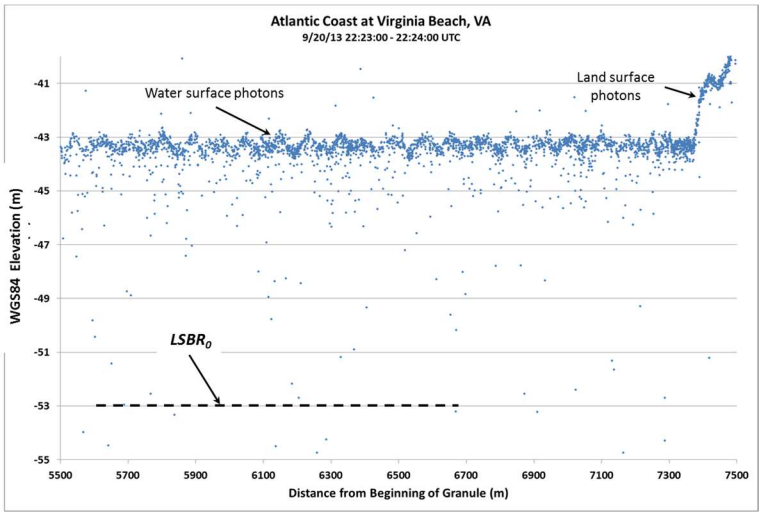

Figure 6-6 Along track profile of MABEL observed photons for Site 2, Atlantic Coast at Virginia Beach. $LSBR_0$ depth indicated at 9.3m below surface. (Jasinski et al., 2016).

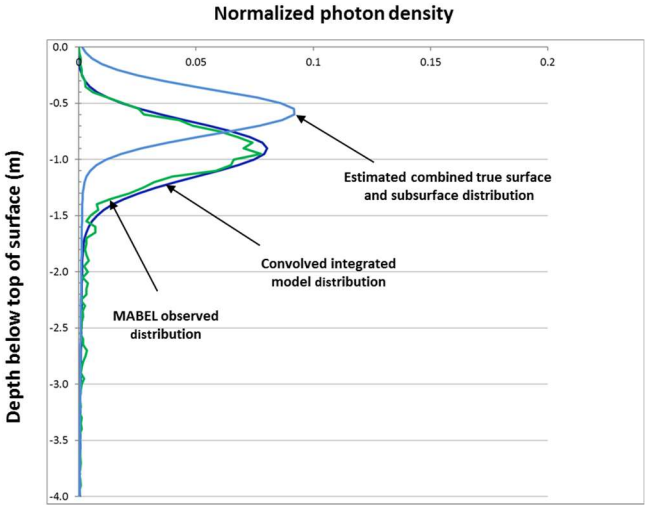

Figure 6-7 Histograms of components of the best fit convolution model for Virginia Beach case.

6.1.3 **Reservoir – Lake Mead**

This case represents a night flight over a relatively clear water body with turbidity equal to 1.6 NTU. The MABEL overpass of February 24, 2012 transected the western portion of Lake Mead in a Southwest to Northeast direction as shown in Figure 6.8. The transect represents two granules of data, or about 2 minutes of acquisition covering about 24 km.

The corresponding plot of the MABEL photons are shown in Figure 12 with the Southwest corner of the lake is on the left. During the flight approximately 91,000 photons were recorded. Because of the nighttime and clear sky conditions, there was an extremely low background count of 0.00008 m^{-2}. The photon cloud data plot and the resulting histograms of the MABEL and model solution are shown in Figures 6-9 and 6-10, respectively.

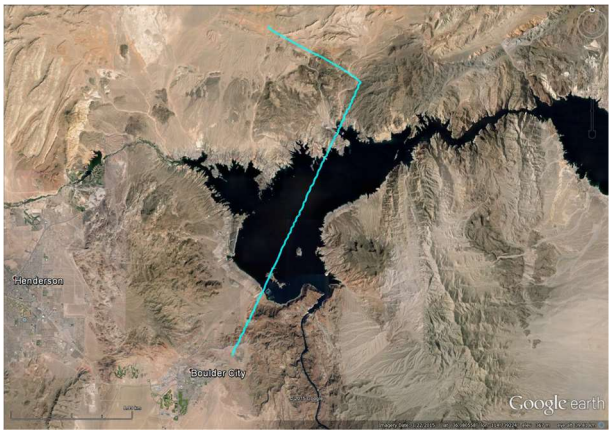

Figure 6-8 Location map of high altitude MABEL flights over Lake Mead in 2012. Base map from Google Earth.

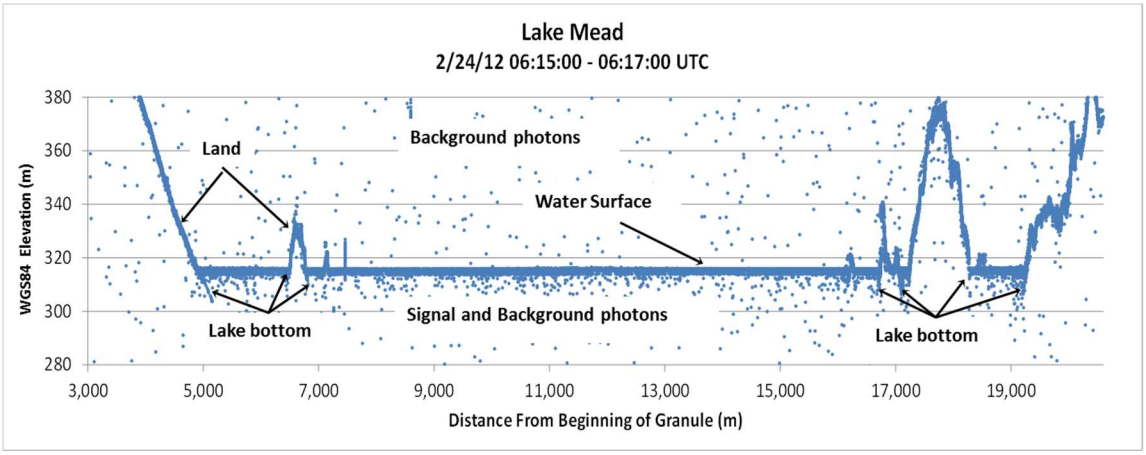

Figure 6-9 MABEL along track photon cloud retrieval from Lake Mead in 2012 (after Jasinski et al., 2016).

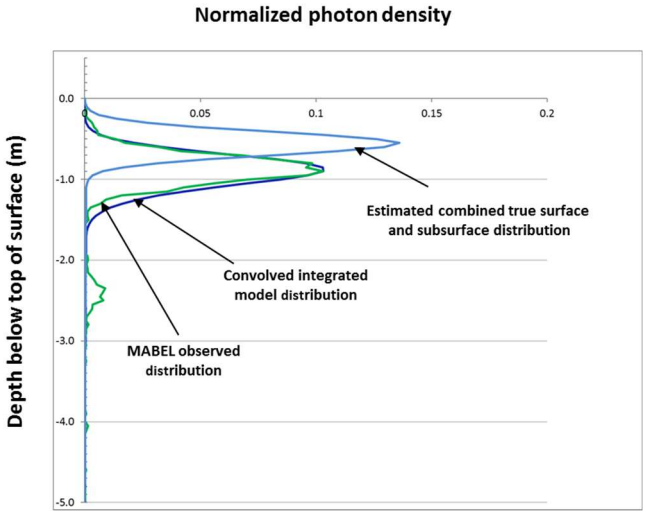

Figure 6-10 Histograms of components of the best fit convolution model for Lake Mead, 2012 case.

MABEL was designed as a high altitude prototype of the ICESat-2 ATLAS sensor, and thus the above results can be expected to be similar to those retrieved from ATLAS.

6.1.4 Bathymetry – Lake Mead

Unlike the previous cases, it was first shown that the bathymetry of Lake Mead is very apparent from MABEL photons in the vicinity of shorelines of many lake edges and islands (Jasinski et al., 2016). To view this more clearly, the southwest shore of Figure 6-9 is expanded in Figure 6-11 below. Prior to plotting, data were first processed to remove an instrument after pulse at about 1.4 m depth. The apparent near-shore bottom of the lake is observed as an extension of the shoreline to a depth of nearly 9 m. True depth would be calculated after correcting for refraction and speed of light.

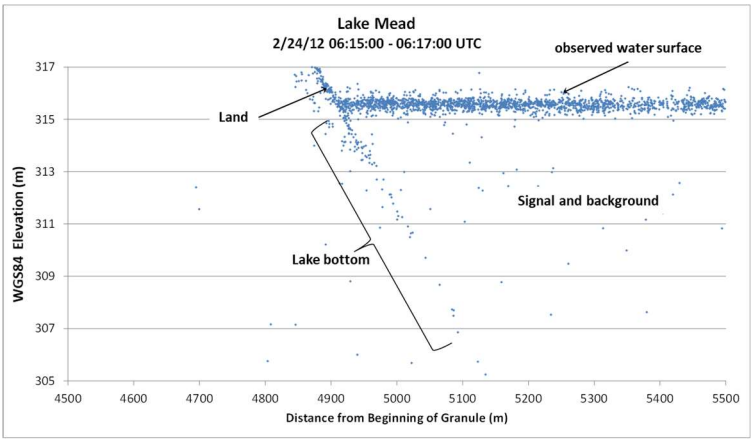

Figure 6-11 Bathymetry of Lake Mead. Expanded view of MABEL photon observations at land water crossing on the southwest shore. Results show penetration of the 532-nm channel into the water column and the presence of lake bottom to a depth of about 10 m.

7.0 REFERENCES

Allen, G.H. and T. M. Pavelsky, 2018: Global extent of rivers and streams. *Science* 361, 585–588. DOI: 10.1126/science.aat0636.

Allouis, T.; Bailly, J.-S.; Lesaignoux, A.; Feurer, D Assessing Water Surface Effects on LiDAR Measurements in very Shallow Rivers: A Theoretical Study Second Space for Hydrology Workshop - "Surface Water Storage and Runoff: Modeling, In-Situ data and Remote Sensing", Geneva (Switzerland), 12-14 November 2007.

Apel, J. R., 1994: An improved model of the ocean surface wave vector spectrum and its effects on radar backscatter. J. Geophys. Res., 99, 16 269–16 291.

ATL03 ATBD, Neumann et al.

Babin, M., and D. Stramski (2005). Variations in the mass-specific absorption coefficient of mineral particles suspended in water. *Limnology and Oceanography*, **49**, 756-767.

Barrick, D.E., Rough Surface Scattering Based on the Specular Point Theory, *IEEE Trans. Antenn. and Propagation*, vol AP-16, pp. 449-454, July 1968.

Barton. J and M. Jasinski, Sensitivity of Depth-Integrated Satellite Lidar to Subaqueous Scattering Remote Sens. 2011, 3, 1492-1515; doi:10.3390/rs3071492, July 2011.

Barton, J, and M. Jasinski (2009), Retrieval of inherent optical properties of turbid coastal waters using active and passive optical remote sensing, IEEE IGARSS, Cape Town, South Africa.

Bascom, W. 1964. Revised and updated edition, 1980. *Waves and Beaches.* Anchor Books, Anchor Press/Doubleday, Garden City, New York, 367 pp.

Bourassa, 1981.

Bourassa, M. A., D. M. Legler, and J. J. O'Brien, 1996: Comparison of ERS scatterometer winds and IMET observations. *Third Workshop on ERS Applications*, IFREMER, June, Brest, 27-42. Also http://coaps.fsu.edu/~bourassa/pubs/SWH_flux/SWH_flux.shtml

Bourassa, M. A., D. G. Vincent, W. L. Wood, 1999: A flux parameterization including the effects of capillary waves and sea state. J. Atmos. Sci., **56**, 1123-1139.

Birkett, C.M. and I.M. Mason, A new Global Lakes Database for a remote sensing programme studying climatically sensitive large lakes, J. Great Lakes Research, 21, No.3, pp.307-318., 1995.

Birkett, C.M., C. Reynolds, B. Beckley, and B. Doorn, From Research to Operations: The USDA Global Reservoir and Lake Monitor, Chapter 2 in 'Coastal Altimetry', Springer Publications, eds. S. Vignudelli, A.G. Kostianoy, P. Cipollini and J. Benveniste, Springer Publications, ISBN 978-3-642-12795-3, 2010.

Breon, F. M., and Henriot, N., Spaceborne observations of ocean glint reflectance and modeling of wave slope distributions, J. Geophys. Res., 111, C06005, doi: 10.1029/2005JC003343, 2006.

Bricaud, A. and A. Morel (1986). Light attenuation and scattering by phytoplanktonic cells: a theoretical modeling, *Applied Optics*, **25**, 571-580.
Buchheim, Oceanography, http://www.marinebiology.org/oceanography.htm.

Bufton, J. L., F. E. Hoge, and R. N. Swift (1983), Airborne measurements of laser backscatter from the ocean surface, Appl. Opt., 22, 2603–2618.

Bukata R P, Jerome J H , Kondratyev K Y and Pozdnyakov D V 1995 Optical properties and remote sensing of inland and coastal waters. CRC Press, 384pp.

Callaghan, A., G. de Leeuw, L. Cohen, and C. D. O'Dowd (2008), Relationship of oceanic whitecap coverage to wind speed and wind history, *Geophys. Res. Lett.*, *35*, L23609, doi:10.1029/2008GL036165.

Calmant, S., Seyler, F., & Cretaux, J. -F. (2008). Monitoring continental surface waters by satellite altimetry. Survey in Geophysics, 29, 247 −269, doi:10.1007/s10712-008-9051-1.

Caulliez, G*., and* C.-A. Guérin *(*2012*),* Higher-order statistical analysis of short wind wave fields*,* J. Geophys. Res*.,* 117*, C06002, doi:*10.1029/2011JC007854.

Churnside, J.H., Konstantin Naugolnykh and Richard D. Marchbanks
" Optical remote sensing of sound in the ocean ", *Proc. SPIE* 9111, Ocean Sensing and Monitoring VI, 91110T (May 23, 2014); doi:10.1117/12.2052930;

Churnside, J.H., V. T.Viatcheslav, and J. J. Wilson, "Oceanographic lidar attenuation coefficients and signal fluctuations measured from a ship in the Southern California Bight," Appl. Opt. 37, 3105--3111 (1998).

E. R. Cook*, R. D. D'Arrigo, M. E. Mann,* J. Clim. 15*,* 1754 *(*2002*).*

Cox, C. and Munk, W.: Measurement of the Roughness of the Sea Surface from Photographs of the Sun's Glitter, J. Opt. Soc.Am., 14, 838-850, 1954.

Cox and Munk, 1953

Dobson et al, 1989

Donelan, M., J. Hamilton, and W. H. Hui, 1985; Directional spectra of wind–generated waves. Philos. Trans. R. Soc. Lond., A 315, 509–562.

Dudis, J., (1986). Electromagnetic Bias of Airborne Off-Nadir Laser Backscatter From the Ocean, J. Geoph. Res., 91, C9, 10750-10752.

Elfouhaily, T., B. Chapron, K. Katsaros, and D. Vandemark (1997), A unified directional spectrum for long and short wind-driven waves, J. Geophys. Res., 102(C7), 15781–15796, doi:10.1029/97JC00467.

Exton RJ, Houghton WM, Esaias WE, Harriss RC, Farmer FH, White HH. "Laboratory analysis of techniques for remote sensing of estuarine parameters using laser excitation". Appl Opt. 1983 Jan 1;22(1):54-64.

Gerstner, F. V. 1802. Theory of waves. Abhandlungen der Koenigl, boehmischen Gesellschaft der Wissenschaften zu Prag.

Gordon, H.R. (1982), Interpretation of airborne oceanic lidar: effects of multiple scattering, *Appl. Opt.* 21, 2996-3001.

Guenther, Gary C. and Thomas, Robert W.L., 1984, Prediction and Correction of Propagation-Induced Depth Measurement Biases Plus Signal Attenuation and Beam Spreading for Airborne Laser Hydrography, NOAA Technical Report NOS 106 Charting and Geodetic Services Series CGS 2.

Guenther, G.C., "Airborne Laster Hydrography: System design and performance factors," NOS, NOAA, Rockville, MD, NOAA Prof. Paper Ser., Mar. 1985.

Guenther, G.C., A. G. Cunningham, P. E. LaRocque, and D. J. Reid, "Meeting the accuracy challenge in Airborne LiDAR Bathymetry," in Proc. EARSel, Dresden, Germany, 2000.

Haltrin, V. I. (2001). *Emperical Relationship Between Aerosol Scattering Phase Funcion and Optical Thickness of Atmosphere Above the Ocean*. Stennis Space Center, MS, CA: Naval Research Laboratory.

Harding, D., and M. J. Jasinski (2004), ICESat observations of inland surface water stage, slope, and extent: A new method for hydrologic monitoring, paper presented at AGU fall meeting, San Francisco, Calif.

Hargreaves, B.R., 2003. Water column optics and penetration of UVR. *UV effects in aquatic organisms and ecosystems 1*, pp. 59-108.

Hasselmann, K, et al., 1973: Measurements of wind-wave growth and swell decay during the Joint North Sea Wave Proj.ect (JONSWAP), Deutch. Hydrogr. Z. Suppl. A8, 12, 95 pp.

Hinzman, L. D., Bettez, N., Bolton, W. R., Chapin, F. S., Dyurgerov, M. B., Fastie, C. L., Griffith, B., Hollister, R. D., Hope, A., Huntington, H. P. et al. (2005). Evidence and implications of recent climate change in northern Alaska and other arctic regions. Clim. Chang. 72, 251-298.

Hu, Y., Stamnes, K., Vaughan, M., Pelon, J., Weimer, C., Wu, D., Cisewski, M., Sun, W., Yang, P., Lin, B., Omar, A., Flittner, D., Hostetler, C., Trepte, C., Winker, D., Gibson, G., and Santa-Maria, M.: Sea surface wind speed estimation from space-based lidar measurements, Atmos. Chem. Phys., 8, 3593-3601, doi:10.5194/acp-8-3593-2008, 2008.

Huang, N. E., 1981: An estimate of the influence of breaking waves on the dynamics of the upper ocean. In Wave Dynamics and Radio Probing of the Ocean Surface, eds O. W. Phillips and K. Hasselmann, Plenum Press, London, UK, 295-312.

Hwang, P.A. 2005: Wave number spectrum mean square slope of intermediate-scale ocean surface waves, J. Geoph Res., 110, C10029, doi:10.1029/2005JC003002.

ICESat-2 Project office, Personal communication.

IPCC, 2014

Jasinski, M. F., J. D. Stoll, D. W. Hancock, Nattala, J., Morison, J., Jones, B., Ondrusek, M., Pavelsky, T., Parrish, C., October 2019. "Algorithm Theoretical Basis Document (ATBD) for Inland Water Data Products, ATL13, **Version 002**, October 1, 2019", NASA Goddard Space Flight Center, 99 pp. https://doi.org/10.5067/3H94RJ271O0C; https://icesat-2.gsfc.nasa.gov/sites/default/files/page_files/ICESat2ATL13ATBDr002mj12202019.pdf. (October 2019a).

Jasinski, M. F., J. D. Stoll, D. W. Hancock, J. W. Robbins, and J. Nattala. 2019. "ATLAS/ICESat-2 L3A Inland Water Surface Height Data Products, ATL13, Version 2." NASA National Snow and Ice Data Center Distributed Active Archive Center, Boulder CO, **Version 2**. https://doi.org/10.5067/ATLAS/ATL13.002 https://nsidc.org/data/atl13/versions/2. (October, 2019b).

M. Jasinski, J. Stoll, D. Hancock, J. Robbins, J. Nattala, T. Pavelsky, J. Morrison, C. Arp, B. Jones, M. Ondrusek, C. Birkett, B. Lehner, and the ICESat-2 Science Team, 2019: Algorithm Theoretical Basis Document (ATBD) for Inland Water Data Products, ATL13, **Version 1**, May 2019, NASA Goddard Space Flight Center, Greenbelt, MD, 89 pp. https://icesat-2.gsfc.nasa.gov/sites/default/files/page_files/ICESat2_ATL13_ATBD_r001.pdf. (May 2019a).

Jasinski, M. F., J. D. Stoll, D. W. Hancock, J. W. Robbins, and J. Nattala. 2019. "ATLAS/ICESat-2 L3A Inland Water Surface Height Data Product, ATL13, **Version 1**." *NASA National Snow and Ice Data Center Distributed Active Archive Center, Boulder CO*, 89 https://doi/10.5067/ATLAS/ATL13.001. (May 2019b).

Jasinski, M.; Stoll, J.; Cook, W.; Ondrusek, M.; Stengel, E., and Brunt, K., 2016. Inland and near-shore water profiles derived from the high-altitude Multiple Altimeter Beam Experimental Lidar (MABEL). *In*: Brock, J.C.;Gesch, D.B.; Parrish, C.E.; Rogers, J.N., and Wright, C.W. (eds.), *Advances in Topobathymetric Mapping, Models,and Applications*. *Journal of Coastal Research*, Special Issue, No. 76, pp. 44–55. Coconut Creek (Florida), ISSN0749-0208.

Jezek, K. C., D. K. Perovich, K. M. Golden, C. Luther, D. G. Barber, P. Gogineni, T. C. Grenfell, A. K. Jordan, C. D. Mobley, S. V. Nghiem, and R. G. Onstott, "A broad spectral, interdisciplinary investigation of the electromagnetic properties of sea ice", *IEEE Transactions on Geoscience and Remote Sensing*, vol. 36, no. 5, pp.1633 -1641, 1998.

Johnsen et al, 1994

Kahma, K.K., 1981, "A study of the growth of the wave spectrum with fetch", J. Phys. Oceanogr., 11, 1503-1515.

Kay, S.; Hedley, J.D.; Lavender, S. Sun Glint Correction of High and Low Spatial Resolution Images of Aquatic Scenes: a Review of Methods for Visible and Near-Infrared Wavelengths. *Remote Sens.* **2009**, *1*, 697-730.

Kay, S., John Hedley, Samantha Lavender, and Alex Nimmo-Smith, "Light transfer at the ocean surface modeled using high resolution sea surface realizations," Opt. Express 19, 6493-6504 (2011) http://www.opticsinfobase.org/oe/abstract.cfm?URI=oe-19-7-6493.

Kirk J T O, 1994, Light and photosynthesis in aquatic ecosystems. Cambridge University Press, Cambridge, 410 pp.

Kwok, R., G. F. Cunningham, S. S. Manizade, W. B. Krabill (2012), Arctic sea ice freeboard from IceBridge acquisitions in 2009: Estimates and comparisons with ICESat, J. Geophys. Res., 117, C02018, doi:10.1029/2011JC007654.

Kwok, R., T. Markus, J. Morison, S. P. Palm, T. A. Neumann, K. M. Brunt, W. B. Cook, D. W. Hancock, and G. F. Cunningham. (2014), Profiling sea ice with Multiple Altimeter Beam Experimental Lidar (MABEL), J. Atmos. Oceanic. Technol., in press..

Lake Access www.lakeaccess.org.

Lancaster, R. S., J. D. Spinhirne, *and* S. P. Palm *(*2005*),* Laser pulse reflectance of the ocean surface from the GLAS satellite lidar, Geophys. Res. Lett., 32, *L22S10, doi:*10.1029/2005GL023732.

Le Méhauté, B. (1976), *An introduction to hydrodynamics and water waves*, Springer, ISBN 0387072322.

Lehner, B. and Döll, P. (2004): Development and validation of a global database of lakes, reservoirs and wetlands. Journal of Hydrology 296/1-4: 1-22.
Liu, P.C., 1970. Some features of wind waves in Lake Michigan. Limnol. Oceanogr., 15:257-72.

Liu, Y., X.-H. Yan, W. T. Liu, and P. A. Hwang, 1997: The probability density function of the ocean surface slopes and its effects on radar backscatter. J. Phys. Oceanogr., 27, 782–797.

Liu, Y., 1996: The spectrum of gravity–capillary waves, the probability density function of ocean surface slopes and their effects on radar backscatter. Ph.D. dissertation, University of Delaware, 140 pp.

Liu, Zhishen, "Estimate of maximum penetration depth of lidar in coastal water of the China Sea", Proc. SPIE 1302, Ocean Optics X, 655 (September 1, 1990); doi:10.1117/12.21476; http://dx.doi.org/10.1117/12.21476.

Longuet-Higgins, M. S., 1963: The generation of capillary gravity waves by steep gravity waves. J. Fluid Mech., 16, 138–159.

Longuet-Higgins, M. S. (1975), On the joint distribution of the periods and amplitudes of sea waves, J. Geophys. Res., 80(18), 2688–2694, doi:10.1029/JC080i018p02688.

Menzies, R. T., *and* D. M. Tratt *(*1997*),* Airborne lidar observations of tropospheric aerosols during the Global Backscatter Experiment (GLOBE) Pacific circumnavigation missions of 1989 and 1990*,* J. Geophys. Res*.,* 102*(*D3*),* 3701–3714*, doi:*10.1029/96JD03405.

Menzies, R.T., David M. Tratt, and William H. Hunt, "Lidar In-space Technology Experiment measurements of sea surface directional reflectance and the link to surface wind speed," Appl. Opt. **37**, 5550-5559 (1998).

Messager, M.L., Lehner, B., Grill, G., Nedeva, I., Schmitt, O. (2016): Estimating the volume and age of water stored in global lakes using a geo-statistical approach. Nature Communications: 13603. doi: 10.1038/ncomms13603.

Mironov, A. S., M. V. Yurovskaya, V. A. Dulov, D. Hauser, and C. A. Guérin (2012), Statistical characterization of short wind waves from stereo images of the sea surface, J. Geophys. Res., 117, C00J35, doi:10.1029/2011JC007860.

Mobley C D 1994 Light and water; radiative transfer in natural waters. Academic Press, San Diego, 592pp. ISBN 0125027508.

Mobley, C.D., G.F. Cota, T.C. Grenfell, R.A. Maffione, W.S. Pegau, D.K. Perovich, 1998. Modeling light propagation in sea ice. IEEE Trans. Geosci. Rem. Sens., 36(5), 1743-1749.

Montes-Hugo MA, Weidemann A, Gould R, Arnone R, Churnside JH, Jaroz E; Ocean color patterns help to predict depth of optical layers in stratified coastal waters. J. Appl. Remote Sens. 0001;5(1):053548-053548-6. doi:10.1117/1.3634055.

Moore, K.D.; Voss, K.J.; Gordon, H.R. Spectral reflectance of whitecaps: Their contribution to water-leaving radiance. *J. Geophys. Res.* **2000**, *105*, 6493-6499.

Monzon, C., Donald W. Forester, Richard Burkhart, and Jim Bellemare »View Author Affiliations, Applied Optics, Vol. 45, Issue 27, pp. 7089-7096 (2006) http://dx.doi.org/10.1364/AO.45.007089

Morel, A., B. Gentili, H. Claustre, M. Babin, A. Bricaud, J. Ras, and F. Tieche, 2007. Optical properties of the "clearest" natural waters. *Limnology and oceanography*, Vol. 52, No. 1, pp. 217-229.

Munk, Walter H. (1950), "Origin and generation of waves", *Proceedings 1st International Conference on Coastal Engineering*, Long Beach, California: ASCE, pp. 1–4, ISSN 2156-1028Munk, W. (1950). "On the wind-driven ocean circulation". *J. Meteorology* **7**: 79–93.

Munk, 1956 referenced in Fig 2-3.

Nagle and White, USGS OFR 2016-1046.

Nayegandhi, A., "Challenges in determining water surface in airborne LIDAR topobathymetry", 15th Annual JALBTCX Workshop, June 2014.

Nave, R., Georgia State University, http://hyperphysics.phyastr.gsu.edu/hbase/waves/watwav2.html.

Pe'eri, S., J.V. Gardner, L.G. Ward, and J.R. Morrison, 1996. The seafloor: A key factor in LiDAR bottom detection. *IEEE Transactions on Geoscience and Remote Sensing*, Vol. 5, pp. 266–1271.

Pe'eri, S., C.E. Parrish, C. Azuike, L. Alexander, and A. Armstrong, 2014. Satellite Remote Sensing as Reconnaissance Tool for Assessing Chart Adequacy and Completeness Information. *Marine Geodesy*, Vol. 37, No. 3, pp. 293-314.

Pe'eri, S., J. V. Gardner, L. Ward, and R. Morrison, The seafloor: a key factor in lidar bottom detection, IEEE Trans. Geo. Rem. Sens., Vol. 49, No. 3, 2011.

Pe'eri, S., Lynnette V. Morgan, William D. Philpot, and Andrew A. Armstrong (*2011*) Land-Water Interface Resolved from Airborne LIDAR Bathymetry (ALB) Waveforms. Journal of Coastal Research: Special Issue 62: pp. 75 – 85.

Peterson, T. C., *et al.,* Recent changes in climate extremes in the Caribbean region, J. Geophys. Res., 107(D21), *4601, doi:*10.1029/2002JD002251, 2002.

Petzold, T.J., (1972) Volume Scattering Functions for Selected Ocean waters. SI) Ref. 72-78, Scripps Inst Ocean., Visibility Lab., San Diego, Calif., 79 pp.

Plant, W. J. (1982), A relationship between wind stress and wave slope, J. Geophys. Res., 87(C3), 1961–1967, doi:10.1029/JC087iC03p01961.

Plant, W. J., A new interpretation of sea-surface slope probability density functions, J. Geophys. Res., 108 (C9), 3295-3298, 2003.

Ross, V., and D. Dion (2007), Sea surface slope statistics derived from Sun glint radiance measurements and their apparent dependence on sensor elevation, J. Geophys. Res., 112, C09015, doi:10.1029/2007JC004137.

Rowland, J. C., *et al. (*2010*),* Arctic Landscapes in Transition: Responses to Thawing Permafrost, Eos Trans. AGU, 91*(*26*),* 229–230, *doi:*10.1029/2010EO260001.

Sathyendranath, S., L. Lazzara, and L. Prieur, Variations in the spectral values of specific absorption of phytoplankton, Limnol. Oceanogr., 32, 403-415, 1987.

Serreze, M. C., Walsh, J. E., Chapin, F. S. III, Osterkamp, T., Dyurgerov, M., Romanovsky, V., Oechel, W. C., Morison, J., Zhang, T. and Barry, R. G. (2000) Observational evidence of recent change in the northern high-latitude environment. Clim. Change, 46, pp. 159–207.

Su W, Charlock TP, Rutledge K., Observations of reflectance distribution around sunglint from a coastal ocean platform. Appl Opt. 2002 Dec 10; 41(35):7369-83.

Tayfun, M. A., 1980. Narrow-band nonlinear sea waves. J. Geophys. Res., 85, 1548-1552.

Tratt, D.M., Robert T. Menzies, Meng P. Chiao, Dean R. Cutten, Jeffry Rothermel, R. Michael Hardesty, James N. Howell, and Stephen L. Durden, "Airborne Doppler lidar investigation of the wind-modulated sea-surface angular retroreflectance signature," Appl. Opt. **41**, 6941-6949 (2002).

Wright, C. W., E. J. Walsh, D. Vandemark, W. B. Krabill, A. W. Garcia, S. Houston, M. Powell, P. Black, and F. D. Marks, 2001: Hurricane directional wave spectrum spatial variations in the open ocean. J. Phys. Oceanogr., 31, 2472-2488.

Wozniak, S. B., AND D. Stramski. 2004. Modeling the optical properties of mineral particles suspended in seawater and their influence on ocean reflectance and chlorophyll estimation from remote sensing algorithms. Appl. Opt. 43:3489–3503.

Wright, C.W., 2014. USGS EAARL-B: Missions, Calibration & Validation. 15th Annual JALBTCX Airborne Coastal Mapping and Charting Workshop, Mobile, AL, 10-12 June: http://shoals.sam.usace.army.mil/Workshop_Files/2014/Day2_pdf/1500_Wright.pdf (last date accessed: 06 Feb, 2015).

Wu, J.: Mean square slopes of the wind-distributed water surface, their magnitude, directionality, and composition, Radio Sci., 25, 37-48, 1990.

Young et al, 1994

Yurovskaya, M. V., V. A. Dulov, B. Chapron, and V. N. Kudryavtsev (2013), Directional short wind wave spectra derived from the sea surface photography, J. Geophys. Res. Oceans, 118, 4380–4394, doi:10.1002/jgrc.20296.

Zaneveld, 2011

Zhang G, Xie H, Kang S, Yi D and Ackley S F 2011 Monitoring lake level changes on the Tibetan Plateau using ICESat altimetry data (2003–2009) Remote Sens. Environ. 115, 1733–42.

Zhang, G.; Hongjie Xie ; Shuiqiang Duan ; Mingzhong Tian and Donghui Yi "Water level variation of Lake Qinghai from satellite and in situ measurements under climate change", J. Appl. Remote Sens. 5(1), 053532 (June 28, 2011). ; http://dx.doi.org/10.1117/1.3601363.

Zhang and Wang, Evaluation of sunglint models using MODIS measurements, J. Quant Spec & Radia. Trans 111(2010) 492-506.